SEDIMENTOLOGY the journal of the International Association of Sedimentologists

*Sedimentology* (2021) **68**, 609–638 doi: 10.1111/sed.12794

# Linking carbonate sediment transfer to seafloor morphology: Insights from Exuma Valley, the Bahamas

JOHAN LE GOFF*, AUDREY RECOUVREUR†, JOHN J.G. REIJMER*, THIERRY MULDER†, EMMANUELLE DUCASSOU†, MARIE-CLAIRE PERELLÒ†, VINCENT HANQUIEZ†, HERVÉ GILLET†, THIBAULT CAVAILHES† and NATACHA FABREGAS†,‡

**College of Petroleum Engineering & Geosciences, Carbonate Sedimentology Group, King Fahd University of Petroleum & Minerals, Building 76, KFUPM, Box 5070, Dhahran 31261, Saudi Arabia (E-mail: jo.le-goff@hotmail.fr, johan.legoff@kfupm.edu.sa)*

*†Université de Bordeaux, CNRS, EPOC, EPHE, UMR 5805, F-33600 Pessac, France*

*‡Department of Earth Science, University of Bergen, Allégaten 41, 5007 Bergen, Norway*

Associate Editor – Tracy Frank

**ABSTRACT**

The depositional record of carbonate slopes provides a valuable archive of past environmental and climatic changes. Modern carbonate slopes reveal morphological variabilities (for example, gullies and canyons) shaped by episodic slope collapses and turbidity currents. Furthermore, climate-induced fluctuations in sea level regulate sediment availability and delivery to the deep-sea. Morphological and climatic controls on calciclastic sediment transfer are often complex to decipher. The aim of this study is to link seafloor morphology and depositional processes in an active carbonate submarine channel (Exuma Valley, the Bahamas) over the last 40 kyr. The dataset includes multibeam and seismic surveys, and two sediment cores retrieved from the valley axis. A series of abrupt slope-breaks, called knickpoints, occurs along Exuma Valley, and plays a key role in sediment transport and accumulation. Initiation processes proposed for knickpoint formation include bank-collapse, side gully erosion and loss of confinement. Slope collapses detected on the bathymetry prevail in the upstream muddy section of the submarine valley, as attested to by a planktic-rich debrite–turbidite couplet in the first core. In contrast, the second core collected downstream of the knickpoints train, includes 32 bioclastic sandy event-beds (i.e. turbidites). Hydrodynamic sorting generates grain segregation (for example, *Halimeda*-rich base versus planktic-rich top) and geochemical contrasts (Sr/Ca) in turbidites. Turbidite frequency and grain composition within beds reflect the variation of carbonate sources during glacial–interglacial periods. This research allows to link slope morphology with deposits of a modern large-scale carbonate factory, and to deduce sea-level changes over that last 40 kyr in the Bahamas. These results can provide new perspectives on the understanding of 'source to sink' mechanisms in carbonate systems.

**Keywords** Carbonates, flow processes, knickpoints, modern environments, sediment transfer, the Bahamas.

## INTRODUCTION

Past and present-day carbonate systems provide an important archive of environmental and climatic changes (Droxler & Schlager, 1985; Roth & Reijmer, 2004; Schlager, 2005; Counts *et al.*, 2019). The past fifty years of research in carbonate sedimentology have demonstrated the importance of slopes as recorders of these past changes. Due to the complex architecture of carbonate slopes, several models were proposed in the literature (Cook *et al.*, 1972; McIlreath & James, 1978; Cook & Egbert, 1981; Mullins & Cook, 1986). Outcrop-based studies conducted on the southern-Tethyan margin in Italy and Albania (Bosellini *et al.*, 1993; Eberli *et al.*, 1993; Hairabian *et al.*, 2015; Le Goff *et al.*, 2015, 2019), on the Pyrenean-Basin margin in Spain (Payros *et al.*, 1999; Drzewiecki & Simo, 2000), and on the Vocontian and Provence basins in France (Everts *et al.*, 1999; Floquet & Hennuy, 2003; Savary & Ferry, 2004; Grosheny *et al.*, 2015), delivered useful observations to predict facies distribution and architecture, otherwise difficult to characterize in the modern ocean (Vigorito *et al.*, 2005; Payros & Pujalte, 2008). An increasing number of studies in modern environments (for example, the Bahamas) involved a combination of seafloor imaging (bathymetry and seismic) with sampling tools in order to refine slope architecture models (Schlager & Ginsburg, 1981; Eberli & Ginsburg, 1987; Mulder *et al.*, 2012, 2017; Jo *et al.*, 2015; Principaud *et al.*, 2015; Tournadour *et al.*, 2017) and sedimentary processes along carbonate slopes (Boardman *et al.*, 1984; Rendle & Reijmer, 2002; Principaud *et al.*, 2016; Chabaud *et al.*, 2016; Wunsch *et al.*, 2018). These recent advances provided a large picture of sediment transfer processes acting on extensive (hundreds of kilometres) carbonate tropical factories from shallow waters (<10 m), to ultra-deep settings (>5000 m; Mulder *et al.*, 2018, 2019).

Sediment transfer from shallow to deep-water was shown to be related to excess carbonate production and slope instabilities (Mullins *et al.*, 1984; Reijmer *et al.*, 1992; Schlager *et al.*, 1994). Excess sediment production and slope instabilities can produce sediment density flows moving downslope with a speed of up to 19 m s$^{-1}$ (Heezen & Ewing, 1952; Talling *et al.*, 2012). These short-lived events can either erode the seafloor, bypass or deposit sediment, shaping submarine slopes (Macdonald *et al.*, 2011; Heerema *et al.*, 2020). Two end-products of density flows are commonly distinguished, namely debrites and turbidites (Bouma, 1962; Hampton, 1972). Debrites are produced by high-density, laminar and cohesive flows where matrix strength favours clast-buoyancy, resulting in poorly sorted deposits. In that case, the movement cessation is assumed to be '*en masse*', or top-down (Mulder & Alexander, 2001b). Turbidites consist of clean, well-sorted (normally or inversely graded), sand-rich beds revealing horizontal-parallel and cross-laminations. Deposition of turbidites is incremental (layer by layer) and results from bed-load traction combined with suspension (Kuenen & Migliorini, 1950; Bouma, 1962).

Density flows along carbonate slopes run through a long-lived network of submarine canyons, channels and gullies (Vigorito *et al.*, 2005; Puga-Bernabéu *et al.*, 2011, 2013; Mulder *et al.*, 2014; Tournadour *et al.*, 2017). Sediment preservation in such deep-water channels is controlled by carbonate production and seafloor morphology (see below).

**1** Tropical carbonate factories such as in the Bahamas, are sensitive to climate (Schlager, 2005; Michel *et al.*, 2018; Laugié *et al.*, 2019). In particular, sea-level fluctuations can either increase or decrease sediment availability, thus impacting subsequent export basinward (Kendall & Schlager, 1981; Droxler & Schlager, 1985; Haak & Schlager, 1989; Counts *et al.*, 2018; Webster *et al.*, 2018). In the Bahamas, sea-level rise and highstand correlate with excess carbonate production in shallow waters, enhancing the export of aragonite and non-skeletal grains to the basin (Kier & Pilkey, 1971; Hine *et al.*, 1981; Droxler *et al.*, 1988; Reymer *et al.*, 1988; Pilskaln *et al.*, 1989; Schlager *et al.*, 1994; Reijmer *et al.*, 2012, 2015). This light-dependent sediment production decreases or ceases when sea level outpaces the production window (Jorry *et al.*, 2010; Paul *et al.*, 2012) leading to platform-drowning (Schlager, 1981; Szulczewski *et al.*, 1996; Ruiz-Ortiz *et al.*, 2004). Emersion of the platform top also results in a shutdown of the factory, leading to karstification and relocation of biogenic producers on the slopes (Haak & Schlager, 1989; Grammer & Ginsburg, 1992; Mindszenty *et al.*, 1995; Mylroie & Carew, 1995; Fouke *et al.*, 1996).

**2** Seafloor morphology of deep-water channels can be impacted by litho-structural contrasts and hydrodynamic processes (Heiniö & Davies, 2007; Mulder *et al.*, 2018). In particular, steep steps in channel gradient, defined as *knickpoints*, have been observed in siliciclastic and carbonate systems (Mitchell, 2004, 2006; Toniolo & Cantelli, 2007; Mulder *et al.*, 2018; Guiastrennec-Faugas *et al.*, 2020). Such seafloor irregularities are thought to modify sediment flow dynamics by governing the erosional and depositional behaviour of the flow (Komar, 1971; Garcia & Parker, 1989; Mulder & Alexander, 2001a; Pohl, 2019). Hence, knickpoints have been suggested to induce rapid transformation of supercritical flows (Fr > 1) into subcritical flows (Fr < 1), generating local scouring (Komar, 1971; Garcia & Parker, 1989; Hiscott, 1994; Slootman & Cartigny, 2020). The loss of lateral confinement leading to *flow relaxation* has shown similar scouring effects in channel–levée transition zones (Pohl *et al.*, 2019).

Despite significant advances in marine research, the link between sediment transfer processes, seafloor morphology and deposits is still poorly constrained in carbonate systems. This is often due to incomplete datasets on morphobathymetry, sediment age-control and preservation. This study uses an unusually complete dataset retrieved from Exuma Valley (the Bahamas) comprising seafloor bathymetry, sub-bottom profiles and sediment cores. The main purpose of this study is to link seafloor morphology and depositional processes in a carbonate submarine channel over the last 40 kyr. The first aim is to characterize knickpoints and their depositional products. The second aim is to document grain sorting in carbonate gravity flows. The third aim is to discuss the effect of sea-level fluctuations related to glacial and interglacial cycles on carbonate production and export.

## GEOLOGICAL SETTING

Exuma Sound (ES), the Tongue of the Ocean (TOTO) and the Columbus Basin are three intra-platform basins dissecting Great Bahama Bank (Fig. 1A). Exuma Sound covers 11 000 km$^2$ and reveals a bowl-shaped morphology along a north-west/south-east axis (Ball *et al.*, 1969). Flat-topped shallow-water lagoons mark the leeward side of low-elevation islands (for example, Long and Cat islands in Fig. 1B). Episodic sediment export from these lagoons [<50 metres below sea level (m b.s.l.)] into the deep basin (1200 to 2000 m b.s.l.) occurs across a steep marginal break (up to 65°) and gullies incising the slope (Crevello & Schlager, 1980; Schlager & Ginsburg, 1981). The downstream end of ES narrows into a major outlet between Cat and Long Island, leading to Exuma Valley (EV; Ball *et al.*, 1969; Mulder *et al.*, 2019).

Slope instabilities were inferred to occur in ES, based on sediment cores described in previous studies. For example, three calciclastic beds were interpreted on the ES basin floor as density flows originating from point-sources at the shelf break (i.e. gullies and slope failures associated with slumping; Crevello & Schlager, 1980). These beds comprise two graded turbidites and one debrite topped with a 2 to 3 m thick turbidite (Crevello & Schlager, 1980). Only the oldest debrite (*ca* 80 to 120 kyr) reached out to the southern part of ES. Further south, slumps, debrites and turbidites were identified on the north-west dipping slope of ES (see IODP – Integrated Ocean Drilling Program – sites 631 to 633 in Fig. 1B; Austin *et al.*, 1986a, 1986b, 1986c; Reymer *et al.*, 1988). Geochemical sediment signatures pointed to a significant increase of platform-derived aragonite during interglacial periods reflecting a highstand shedding of shallow-water banks (Droxler & Schlager, 1985; Reymer *et al.*, 1988).

Exuma Valley (EV; 2000 to 3200 m b.s.l.) is 130 km long and prolongs ES towards Exuma Canyon (3200 to 4500 m b.s.l.), leading to the San Salvador abyssal plain (>4500 m b.s.l.; Mulder *et al.*, 2019). Six knickpoints have been identified in the EV axis (Mulder *et al.*, 2019). Sediment sources for EV come from the upper slopes of islands, cays and relict platforms (Fig. 1; Mulder *et al.*, 2019). The products of density flows were collected in the axis of EV and spill-over levées. Coarse-grained, poorly sorted deposits and sand-rich deposits interbedded with carbonate ooze were identified in these environments (Mulder *et al.*, 2019). This study focuses on the upper 60 km of the valley (Fig. 1).

## METHODOLOGY

The Carambar 2 cruise explored Exuma Sound (ES) and Exuma Valley (EV) down to the San Salvador Abyssal Plain (Fig. 1; Mulder *et al.*, 2019). High-resolution multibeam imaging [Kongsberg EM122/EM170 (Kongsberg Gruppen ASA, Kongsberg, Norway)] and sub-bottom seismics were acquired (*Chirp* profiler, 1.8 to 5.3 kHz). Sediment cores were retrieved with a Küllenberg gravity-device and analyzed for grain

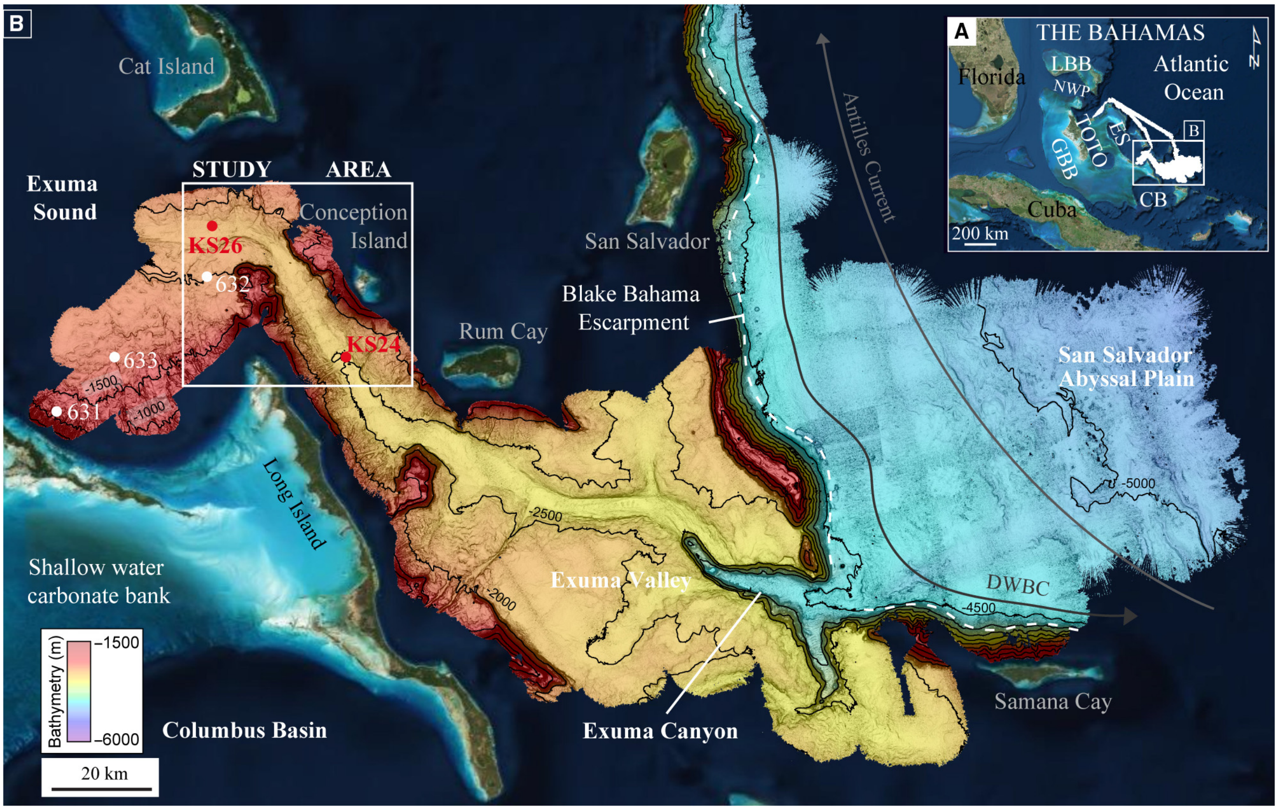


**Fig. 1.** Location map of the study area. (A) The Bahamas in the Caribbean Sea, and neighbouring landmasses. Location of Exuma Valley (EV) indicated with a white square. LBB, Little Bahama Bank; NWP, Northwest Providence Channel; TOTO, Tongue of the Ocean; GBB, Great Bahama Bank; ES, Exuma Sound; CB, Columbus Basin. White-coloured area: Carambar cruise research area. (B) Bathymetric map of EV and main physiographic elements. Location of the study area indicated with a white square. Location of the studied cores (KS26 and KS24) and ODP cores (631 to 633) are indicated. DWBC, Deep-Water Boundary Current.

composition, geochemistry [X-ray fluorescence core scanner (XRF), 10 kV, 30 kV] and acoustics [Geotek Multi-Sensor Core Logger (MSCL); Geotek Limited, Daventry, UK]. These datasets were integrated to provide a comprehensive review of seafloor morphology, sediment transfer and resulting products in EV.

## Seafloor morphology

Geometrical and statistical analyses performed on seafloor bathymetry, backscatter and slope data were conducted using ArcGIS 10.5 (Figs 1 to 4). A classification of seismic echofacies was performed on the study area based on Recouvreur (2017). Special attention was given to the morphology of knickpoints (Mitchell, 2004, 2006). Features described on the knickpoints include a vertical drop, an average and maximum inclination of the slope face, and an upper/lower slope-break angle (alternatively dipping downstream or upstream; Fig. 5A).

## Sediment core collection and logging

Sediment cores KS26 (349 cm) and KS24 (587 cm) were retrieved at 2211 m and 2497 m b.s.l. in the upper part of EV (Fig. 1B). The cores were positioned on the seismic profiles using a P-wave velocity of 1600 m $s^{-1}$ obtained from the MSCL results on KS24, in accordance with Anselmetti & Eberli (1993). The cores were split lengthwise, photographed, described and X-rayed [Scopix sourced with 160 kV, 19 mA; Migeon *et al.*, 1998]. Sediment descriptions distinguished carbonate ooze (O) from sandy deposits (T) and muddy rubble (D) (Droxler & Schlager, 1985; Reymer *et al.*, 1988): T-beds and D-beds were used to infer sediment provenance and settling processes. Carbonate O-intervals

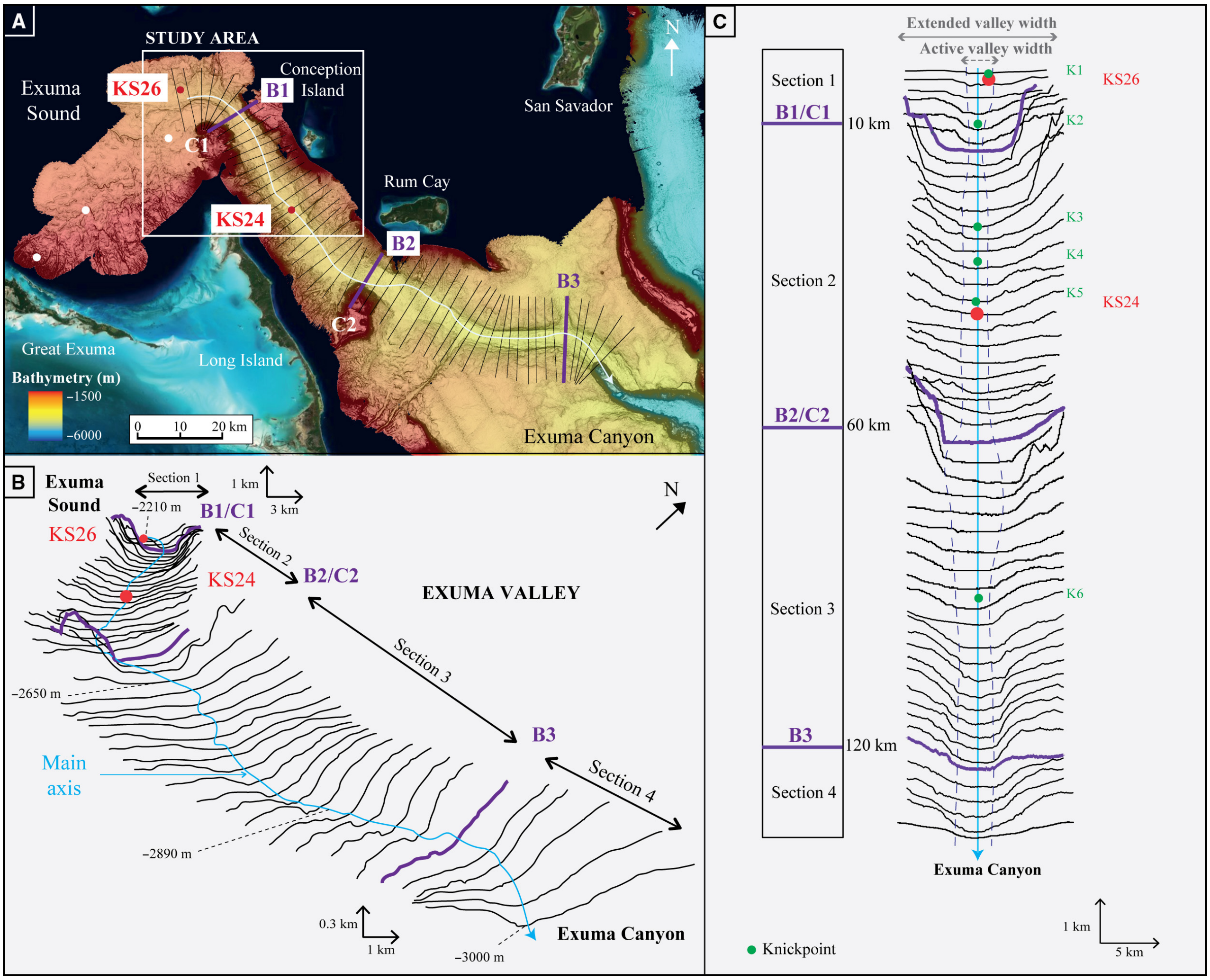


**Fig. 2.** Morphology of Exuma Valley (EV). (A) Location of slope profiles, shown in (B) and (C), and core locations KS26 and KS24. White dots correspond to ODP cores (see Fig. 1). Study area marked by white square. 'B', bend; 'C', constriction. (B) Three-dimensional view of bathymetric slope sections in EV. (C) Slope profiles oriented normal to the valley axis and location of each section of EV. Active valley width indicated as well as the location of the sediment cores (KS26 and KS24) and knickpoints (K1 to K6).

were used to constrain depositional timing. A decimetre sampling step was applied to T-beds and D-beds for grain-size and point counting, whereas O-intervals were sampled at their upper and lower limit for dating.

## Grain-size measurements

Laser diffraction analysis (Malvern *Mastersizer 2000G*; Malvern Panalytical, Malvern, UK) was performed to determine grain-size fractions ranging from 0.02 to 2.0 mm. Coarse samples (>800 µm, typically the T-beds and D-beds) were further analyzed using eight sieves (mesh size ranging from 800 to 10 000 µm). Note that the Malvern *Mastersizer 2000G* commonly detects the largest dimension of small particles (x, y, z) thus leading to an overestimation of elongated particles (for example, aragonite needles). Hence, the upper clay-size limit is fixed at 10 µm (Fauquembergue *et al.*, 2018). In total, 33 (KS26) and 82 samples (KS24) were selected in the T-beds and D-beds, as well as eight (KS26) and 26 samples (KS24) in the O-intervals. Numerical grain-size integration of laser diffraction and mechanical sieving was performed following the method described in Dinis & Castilho (2012).

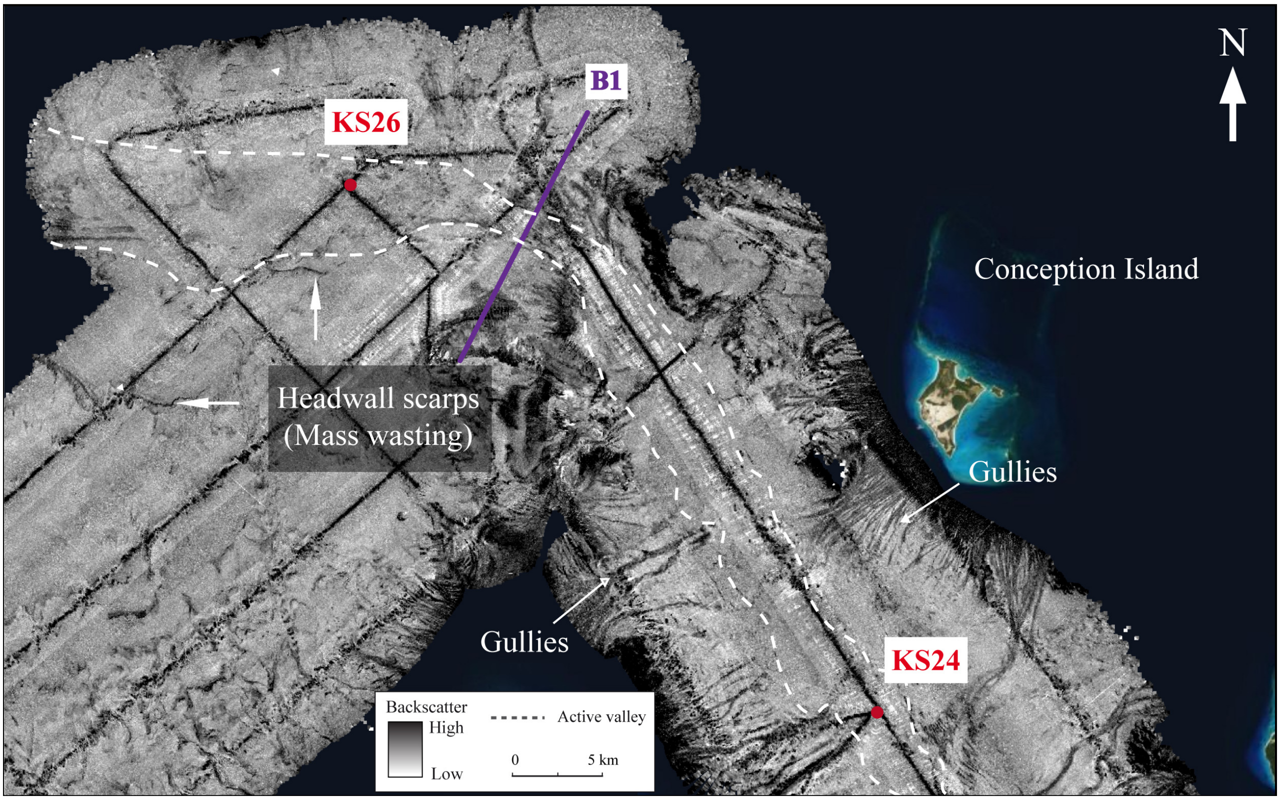


**Fig. 3.** Backscatter imaging of the study area. Active valley width is highlighted with white dash-lines. Red dots correspond to sediment cores KS26 and KS24. The first bend (B1) separates section 1 (upslope) from section 2 (downslope).

## Point counting

Point counting was focused on T-beds and D-beds which included particles larger than 2 mm to facilitate the identification. Up to nine fractions were obtained for each sample and examined under a binocular reflected light microscope (eight and 21 samples for KS26 and KS24, respectively). For example, D1 in KS26 was studied at four stratigraphic positions to understand particle sorting at the bed scale. The total number of grains for each fraction was counted except for the fraction <800 μm. Skeletal grains were identified to the group level (corals, ostracods, bivalves, planktic foraminifera, benthic foraminifera, pteropods, etc). For non-skeletal grains (for example, mud clasts and aggregates), a few representative constituents were routinely identified in order to determine their provenance. For example, an aggregate consisting of ooids or planktic foraminifera would indicate an outer shelf versus basinal environment, respectively. Grain composition was normalized for each stratigraphic position, and presented in a single plot for each sediment core. Additionally, a semi-quantitative evaluation of the grain-composition (for example, shelf-derived or slope-derived) was performed for 14 (KS26) and 24 samples (KS24) retrieved from O-intervals.

## Micropalaeontological analyses

Micropalaeontology was performed on O-intervals after washing with deionized water over a sieve of 150 μm, drying and counting. Particular interest was given to the *Globorotalia menardii* complex (i.e. *menardii* d'Orbigny, *tumida* Brady, 1877; and *flexuosa* Koch, 1923) to determine interglacial (for example, Marine Isotopic Stage 1 – MIS1) and glacial intervals (for example, MIS2–MIS3; Ericson *et al.*, 1964; Ericson & Wollin, 1968). In addition, identification and counting of *Globorotalia truncatulinoides* (dextral and sinistral, d'Orbigny, 1839) and *Pulleniatina obliquiloculata* (Parker & Jones, 1865) helped to refine time-constraints. The glacial–interglacial

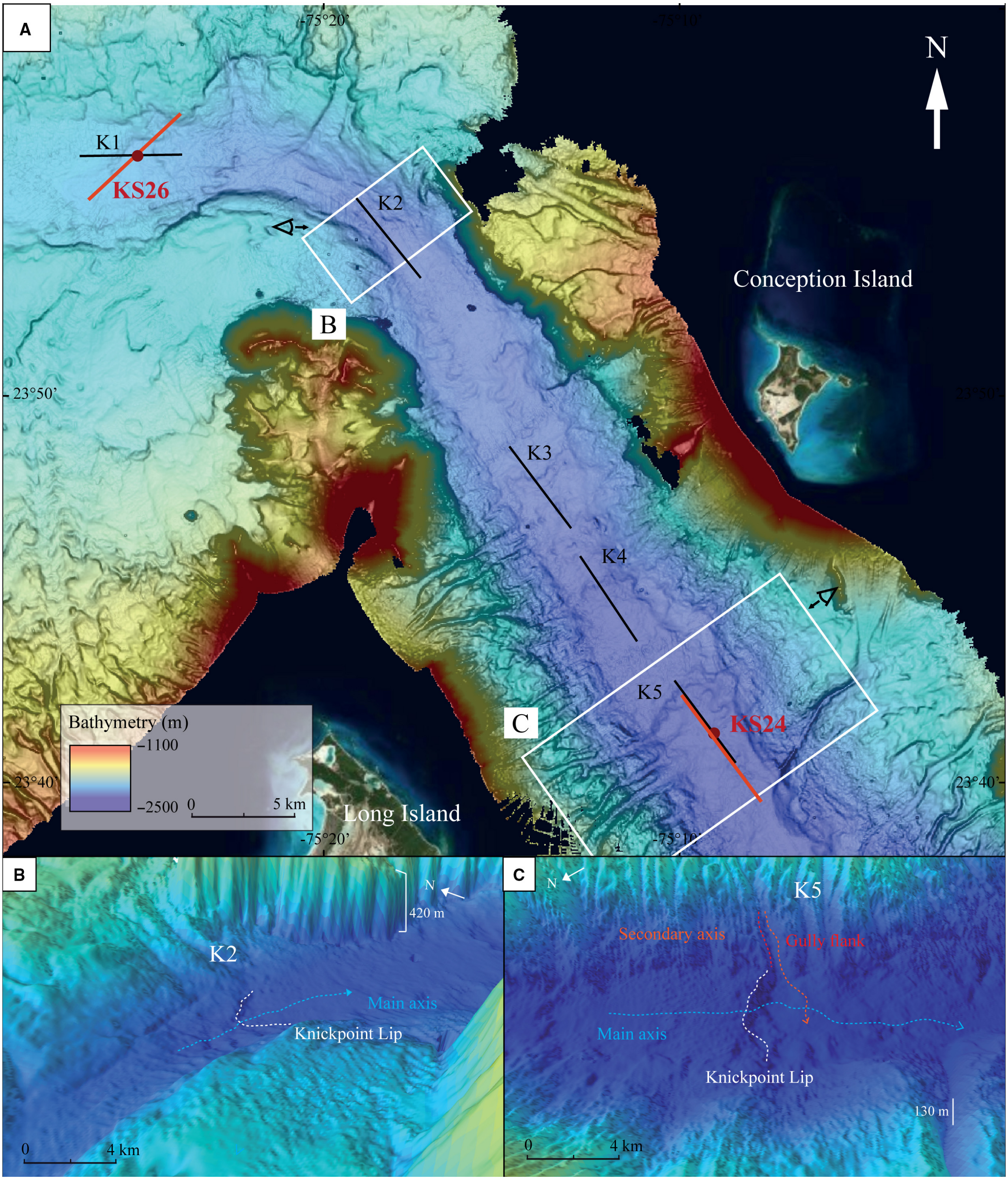


**Fig. 4.** (A) Morphobathymetry study area. Sediment cores and knickpoint locations are indicated. Black lines show the slope profiles presented in Fig. 5 while red lines show the seismic lines presented in Fig. 6. (B) Close-up on the spoon-shaped morphology of K2 at the loss of confinement of the valley. (C) Close-up on a gully-related knickpoint (K5). Figure produced with ARCSCENE 10.5 (ESRI, 2020).

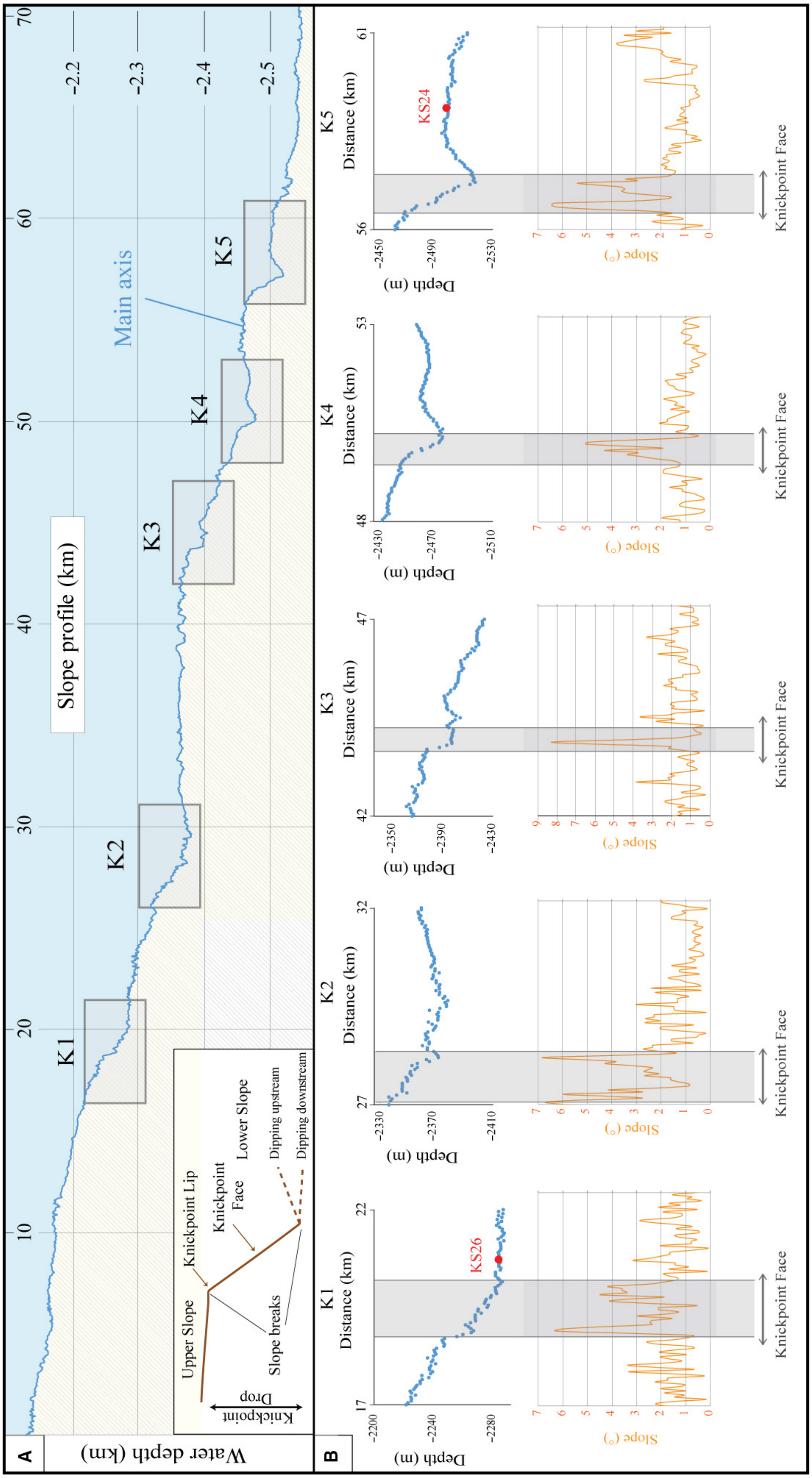


**Fig. 5.** (A) Slope profiles and slope angles for the five knickpoints (K1 to K5) identified in the study area and terminology associated with knickpoints. (B) Measurements related to the geometry of the knickpoints, for example, morphology and slope angles. Positions of sediment cores KS26 and KS24 are indicated.

nature of the deposits was analyzed using the dextral versus sinistral occurrences of *Globorotalia truncatulinoides* (Chabaud, 2016). The absence of *Pulleniatina obliquiloculata* during Marine Isotopic Stage 3 (MIS3; Rama-Corredor *et al.*, 2015) improved the stratigraphic timeframe of the studied cores.

### Age of sediment

Radiocarbon dating was performed for three samples collected from each core. Sampling was focused on O-intervals showing a dominant planktic signal (foraminifera and pteropods). *Globigerinoides* sp. were preferentially targeted in order to avoid foraminifera species living below the thermocline, hence not in equilibrium with atmospheric carbon (Rebotim *et al.*, 2017). Analyses were performed by Beta Analytics (Miami, FL, USA). A reservoir age of 400 years was applied to the results. Conventional ages were calibrated using CALIB 7.0.4 (Stuiver *et al.*, 2013) and the MARINE13 curve (Reimer *et al.*, 2013).

### Strontium to calcium ratios

Strontium (Sr) and calcium (Ca) concentrations were acquired at a centimetre-scale resolution with an XRF core scanner for KS24. Strontium was demonstrated as a proxy for aragonite content in tropical carbonate factories (Counts *et al.*, 2019). Aragonite content is widely used as a proxy for glacial and interglacial cyclicity (Droxler & Schlager, 1985; Roth & Reijmer, 2005). In this study, Sr/Ca ratios were thus used to distinguish carbonates deposited during interglacial periods (i.e. aragonite, Sr-rich) versus glacial periods (i.e. aragonite, Sr-poor; Boardman & Neumann, 1984; Droxler & Schlager, 1985; Reymer *et al.*, 1988). Diagenetic dissolution of aragonite is discarded in the studied sediments (collected at 2211 m b.s.l. and 2497 m b.s.l.) given their young age (<42 kyr) and the particularly deep aragonite compensation depth in the Bahamas (*ca* 4000 m b.s.l.; Droxler *et al.*, 1988).

## RESULTS

### Geomorphology

The following section focuses on the morphology of Exuma Valley (EV), with a particular focus on the knickpoints covering the valley floor.

*General overview*

Major constrictions and inflexions punctuate the 130 km long course of Exuma Valley (EV; Fig. 1B). Constrictions C1 and C2 are located to the north-west and south-west of Conception Island and Rum Cay, respectively, and match two of the three major bends in EV (B1, B2 and B3; Fig. 2A). These bends subdivide EV into four morphological sections (Table 1; Fig. 2B and C). Average sinuosity in the main axis of EV is very low and decreases progressively downslope (Table 1). Sinuosity ranges from *ca* 1.2 for section 1 situated in the curvy outlet of ES, down to *ca* 1.0 for sections 3 and 4 in the downslope part of EV (Table 1; Fig. 2). Slope profiles across EV show a flat bottom confined between >2° slope angle levées (Fig. 2B and C). The flat portion in the axis defines the *active valley* width as opposed to the *extended valley* width which extends from the levées to the outer rim of flat-topped platforms (Figs 1 and 2). The *active valley* widens downslope from 1.9 km (section 1) to 4.7 km (section 2). It narrows to 3.7 km at the second constriction (C2), and widens to 6.3 km and 5.8 km (sections 3 and 4; Table 1; Fig. 2). The absence of confinement and low-angle slopes inclined towards the EV-axis in sections 3 and 4 coincides with a significant enlargement of the *extended valley* width (Table 1; Fig. 2).

**Table 1.** Morphological characterization of Exuma Valley.

| Morphology | Location along the valley (km) | Active valley width (km) | Extended valley width (km) | Sinuosity | Incremental sinuosity |
|---|---|---|---|---|---|
| Section 1 | 0–10 | 1.9 | >20 | 1.21 | 1.21 |
| Section 2 | 10–57 | 1.9–4.7 | 1.9–4.7 | 1.06 | 1.10 |
| Section 3 | 57–120 | 3.7–6.3 | >20 | 1.03 | 1.07 |
| Section 4 | >120 | 3.7–5.8 | >20 | 1.04 | 1.07 |

 

Backscatter imaging display contrasted morphological features between section 1 and section 2 (Fig. 3). Section 1 comprises gently dipping flanks (<5° angles) incised by a few headwall scarps (16° slope angle, and up to 302 m high) resulting from slope collapses (Fig. 3). Section 2 shows straight-lined gullies incising the steep slopes (>25°) of Long Island, Conception Island and Rum Cay.

*Knickpoints*

The prevailing flat longitudinal profile of EV is characterized by slope irregularities, called knickpoints (Figs 4 and 5). Major knickpoints occur at six locations along the course of EV (K1 to K6; Mulder *et al.*, 2019), among which five are identified in the study area, in the upper part of the valley (K1 to K5; Fig. 4A). In section 1, K1 and K2 are respectively located 0.3 km upslope and 12.8 km downslope of KS26 (Fig. 2C). In section 2, K3 to K5 are all situated upslope of KS24, K5 being the closest to the core location (*ca* 2.5 km; Fig. 2C). The bathymetric drop of the seafloor in the valley axis is *ca* 350 m between K1 at 2170 m b.s.l. to K5 at 2520 m b.s.l. Individual knickpoints have a bathymetric drop ranging from 7 m for K2 to 50 m for K5 (Fig. 5).

In plan-view, K2 displays a crescentic spoon shape, favouring flow convergence, followed by an enlargement of the active valley (Fig. 3). Kilometre-scale seafloor lineations along the valley axis are visible upstream of K2 (Fig. 4A). Other knickpoints show an irregular (K1 and K3) to slightly crescentic shape (K4 and K5) in plan-view (Fig. 4A and B). The slope angle of knickpoint faces is *ca* 7° for K3, K4 and K5, and *ca* 3 to 4° for K1 and K2 (Table 2). The upper slope is similar for all knickpoints (2.5 to 3.7°; Table 2), while the lower slope ranges between 1.6° (K1, dipping downstream) and 1.7° (K2 to K5, dipping upstream; Table 2; Fig. 5A and B).

Three categories of knickpoints are recognized based on their: (i) direct; (ii) partial; or (iii) absence of connection with flank-adjacent gullies transiting perpendicular to the valley axis (Fig. 4). The first category includes K5, which is directly connected to a gully incising the slope of Long Island (Fig. 4C). The second category comprises K3 and K4 showing a less pronounced connection to gullies. The third category includes K1 and K2 because there is no link between the gully and their morphology (Fig. 4A).

## Sedimentary record

Sub-bottom profiles and two sediment cores were collected to characterize the composition of the seabed described above. The first core (KS26) is located 0.3 km downstream of knickpoint K1 while the second core (KS24) is located 2.5 km downstream of knickpoint K5 (Fig. 4A).

*Seismic echofacies and depositional architecture*

Core KS26 is located in a topographic depression (Fig. 6A) while KS24 is situated at the top of a topographic high (Fig. 6B). Three echofacies were tied to three types of sediment facies in the cores (Fig. 6).

**1** High-amplitude, continuous reflection characterizing the uppermost metre in both cores corresponds to sediment facies dominated by O-intervals (Fig. 6).

**2** Low-amplitude, semi-continuous to discontinuous reflection is seen from 1.0 to 2.6 m in KS26 and 1.0 to 5.9 m in KS24, which corresponds to O-intervals and sandy T-beds (Fig. 6).

**3** Diffuse acoustic facies characterizes a rubble D-bed in KS26, from 2.6 m down to the core bottom (Fig. 6A). This diffuse acoustic facies exceeds the core length by far, and is limited below by a *ca* 500 m long, semi-continuous reflection positioned at an estimated depth of 14 m (Fig. 6A).

**Table 2.** Morphological characteristics of knickpoints (KN) K1 to K5.

| | K1 | K2 | K3 | K4 | K5 |
|---|---|---|---|---|---|
| Upper slope-break (°) | 2.50 | 3.64 | 3.61 | 3.96 | 3.73 |
| KN drop (m) | 15 | 7 | 25 | 28 | 50 |
| KN face average slope (°) | 2.5 | 3.6 | 3.6 | 4.0 | 3.7 |
| KN face max slope (°) | 3.1 | 4.1 | 7.0 | 6.8 | 6.9 |
| Lower slope-break (°) | 1.59 | −1.45 | −1.54 | −1.27 | −1.69 |

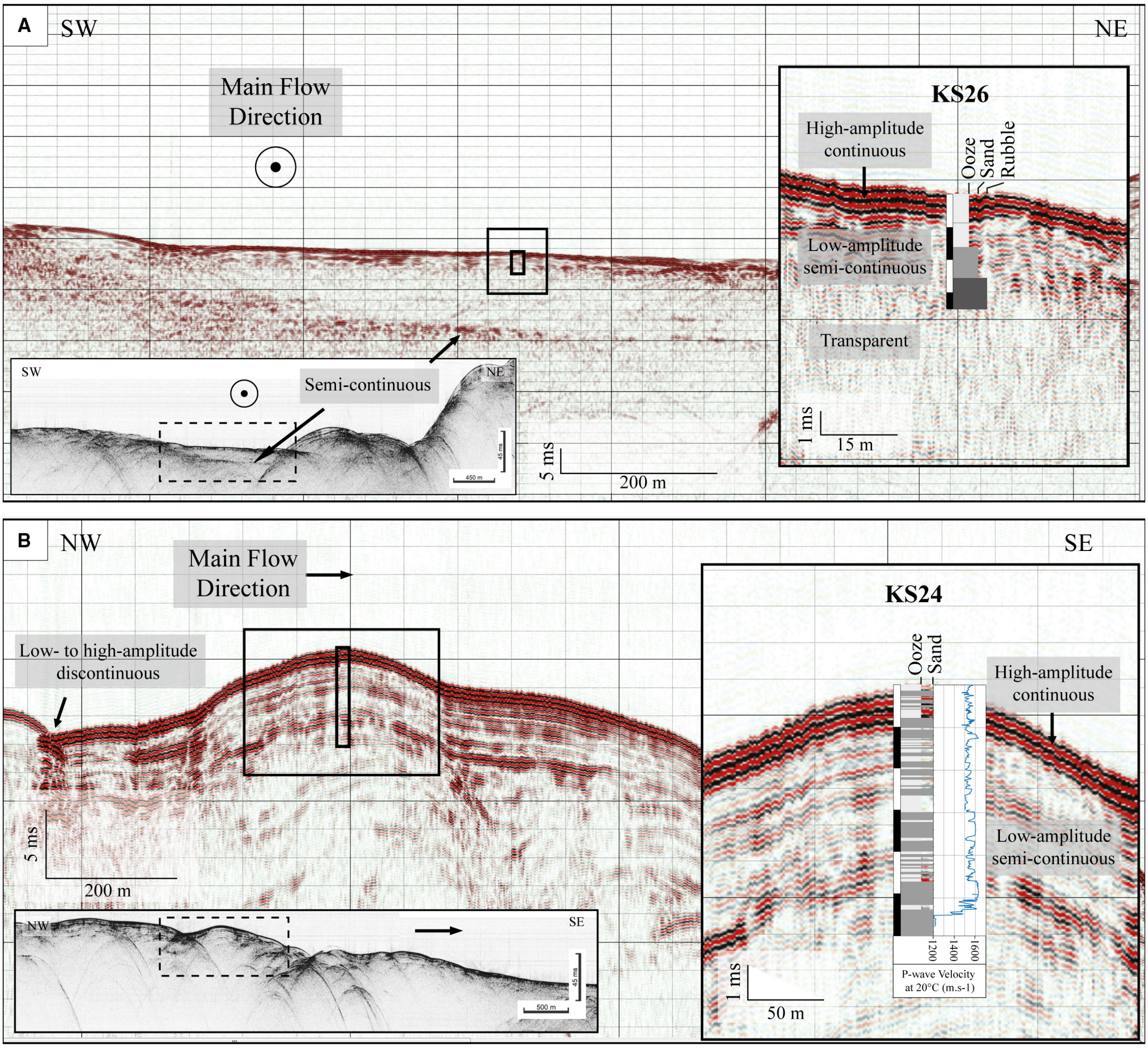


**Fig. 6.** Very high-resolution seismic (*Chirp*) imaging and associated core sediment calibration for KS26 (A) and KS24 (B). Large-scale inset at the bottom left and close-up to the right. Black and white scales to the left of each core are in metres. P-wave velocity (m s$^{-1}$) is plotted next to KS24.

## *Sedimentological descriptions*

The depositional record of KS26 and KS24 comprises ooze intervals (O), as well as sand-rich and rubble-rich beds (T-beds and D-beds, respectively) incrementally numbered from the top (younger deposits) to the base (older deposits).

## *Depositional record of KS26*

Core KS26 comprises five stratigraphic divisions here described from the oldest (D1 at the base) to the youngest (O1 at the top; Fig. 7). D1 shows a crude fining-upward trend ranging from sub-rounded boulder-sized clasts at the core bottom, to pebble-sized clasts at the top (Figs 7 and 8A). These boulder and pebble-sized clasts are surrounded by smaller clasts (*ca* 1 cm ø, making up 65 to 78% of the grains) and loose skeletal grains (Figs 8A and 9). All clasts consist of planktic biota (foraminifera and pteropods, *ca* 63 to 150 μm) embedded in carbonate silts and mud (0 to 63 μm) (Fig. 8A). Combined fractions of bivalve shells, *Halimeda*, benthic foraminifera (for example, *Amphistegina lessonii*, d'Orbigny in Guérin-Méneville, 1832) and echinoderm

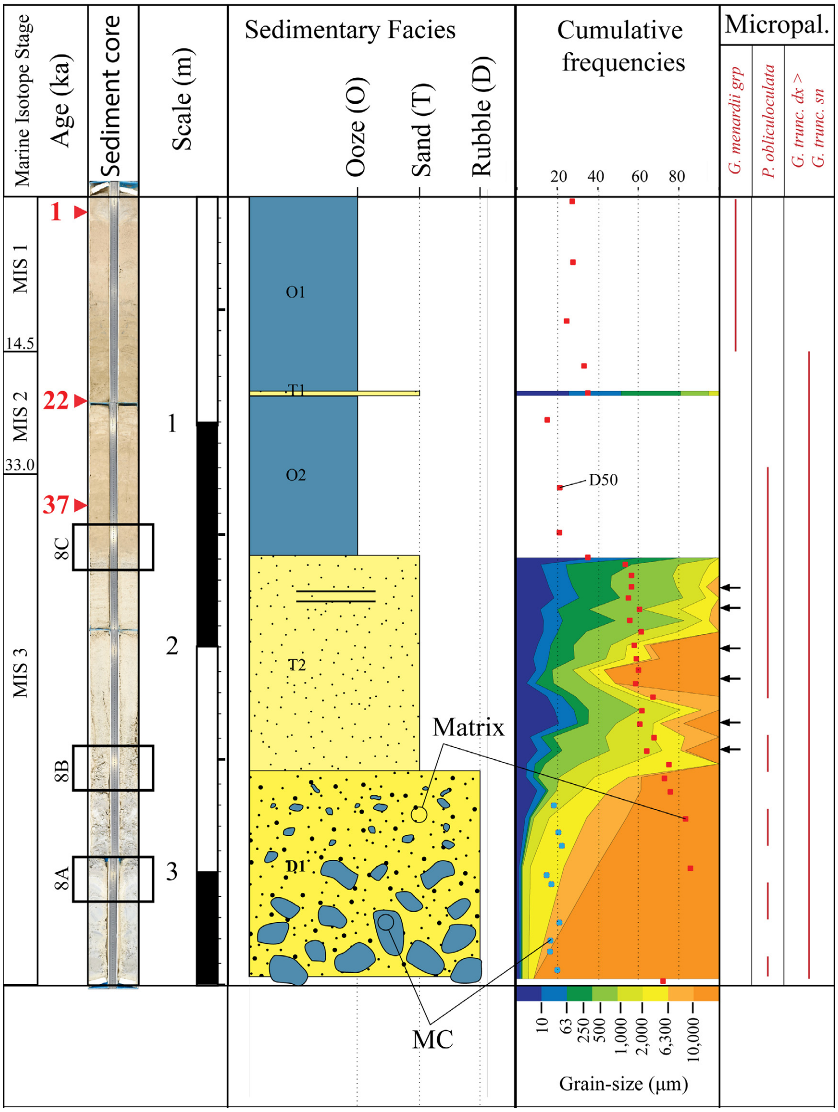


**Fig. 7.** Sediment core KS26. Left to right: proposed age model of the deposits according to biostratigraphy and radiocarbon dating (red arrows); core photograph with black boxes referring to Fig. 8, scale (in metres); simplified representation of the core with interval coding; cumulative grain-size frequencies for each sample (grain-size pulses represented with black arrows); median grain-size (D50, red squares) and micropalaeontology. MC, mud clasts.

fragments become substantial at the top of D1 and base of T2 (6 to 12%; Fig. 9).

The transition from D1 to T2 is picked at the grain-size break occurring within a narrow interval (257.5 to 251.5 cm; Fig. 7) showing no evidence for erosion or colour variation (Fig. 8B). Loose planktic grains and very-fine sands become progressively dominant in T2 at the expense of mud clasts, which become smaller and form only 5% of the grains at the top of T2 (centimetre to millimetre size; Figs 8B, 8C and 9). Coarser sediments (i.e. >1 cm) abruptly disappear from the assemblage at the base of T2 while they form *ca* 40% of the cumulative grain frequencies at the top of D1 (Fig. 7). The number of aggregates is negligible in D1 (<2%) and reach up to 12% in the upper part of T2 (Fig. 9).

Grain-size analyses along T2 (94 cm thick) reveal two 40 to 50 cm thick upward-fining sequences (Fig. 7). Mud-size and silt-size proportions (<63 µm) increase towards the top of each sequence, while coarser fractions decrease (Fig. 7). These two sequences are abruptly segregated by a grain-size pulse with very-coarse to pebble-sized particles making up 60% of the total grain-size assemblage (210 cm; Fig. 7). Smaller grain-size pulses appear between 245.5 cm and 172.5 cm along the core (Fig. 7). Horizontal parallel laminations occur in the upper part of T2, as shown in X-ray photographs (Fig. 8C).

Intervals O1 and O2 at the upper part of KS26 show two metre-thick intervals mainly consisting of planktic grains and carbonate mud, separated by a centimetre-thick sandy bed (T1;

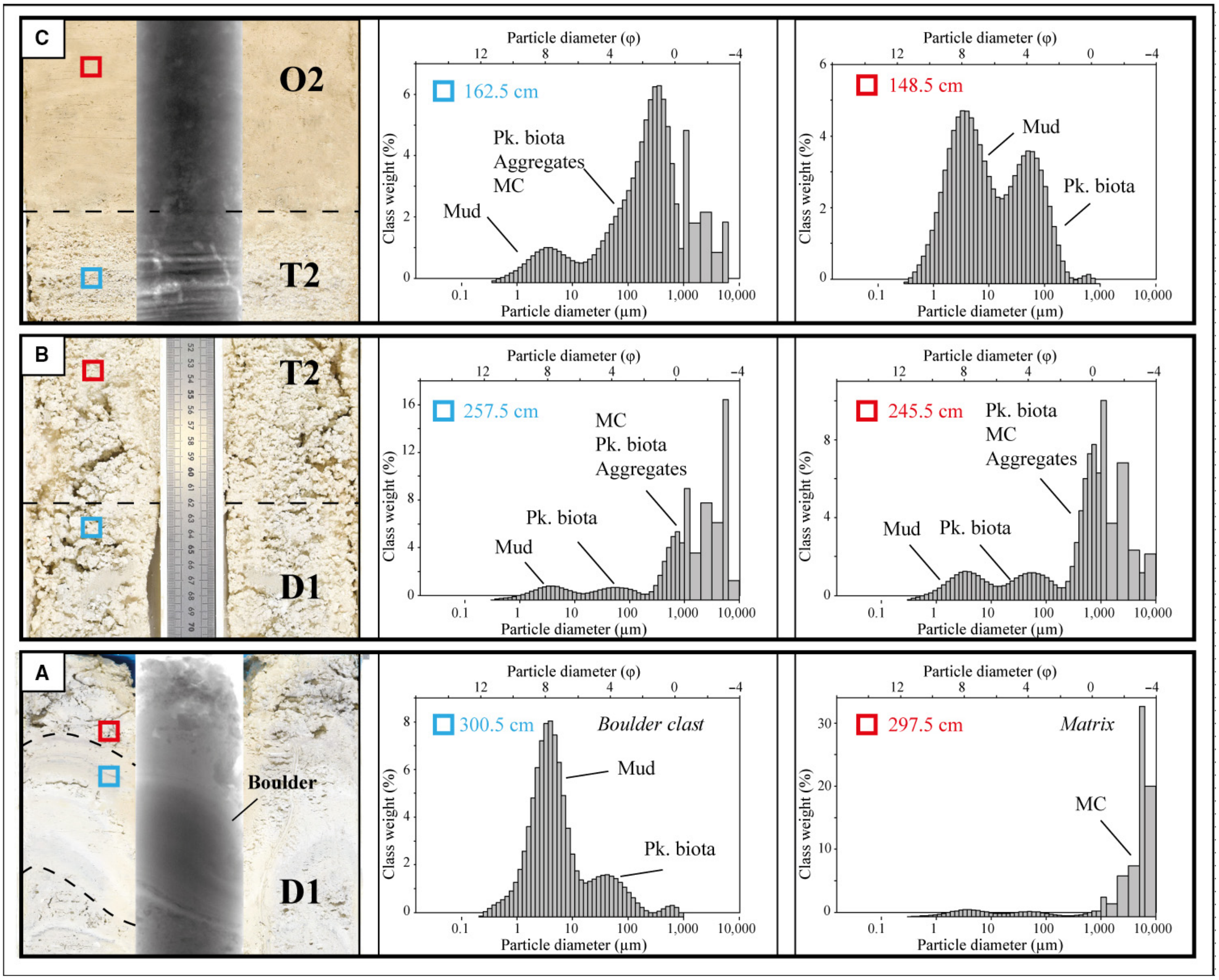


**Fig. 8.** High-resolution photographs of KS26 for stratigraphic positions shown in Fig. 7. Particle diameter and their respective percentage within the total assemblage. Blue and red squares show the location each sample. Differences between grain-size classes are inherent to the measurement method, laser or sieving. Planktic biota includes planktic foraminifera and pteropods. MC, mud clasts; Pk, planktic. The panels on the far-left hand-side are 20 cm across.

Fig. 7). O-intervals reveal a D50 grain size of *ca* 63 μm (Fig. 7), a bimodal distribution matching mud-sized to silt-sized particles (0 to 63 μm), and loose foraminifera and pteropods (63 to 150 μm) (Fig. 8B and C). T1 has a similar composition to O1 and O2, with a significant proportion of loose planktic grains at the expense of the mud content (Fig. 7).

## *Depositional record of KS24*

Core KS24 is made of alternating T-beds and O-intervals (32 in total) with a sand to mud ratio of *ca* 60% (Fig. 10). The core bottom shows the thickest sandy beds, i.e. 54 cm and 60 cm thick for T31 and T32, respectively (Fig. 9). The coring device could not reach the base of T32, likely because of coarse skeletal particles (>1 cm; Figs 10 and 11A) obstructing further penetration. Carbonate O-intervals are generally thinner than T-beds, the thickest one reaching 29.5 cm (O21). Grain-size analyses show unimodal distributions for T-beds with a negligible amount of silt and mud, while bimodal distributions characterize O-intervals. The latter are mainly composed of planktic biota combining silt and mud fractions, and with variable, minor occurrences of shelf derived skeletal debris (Fig. 11B and C).

A general upward-fining trend is observed in all T-beds as shown by the D50 trend (Fig. 10). The thickest T-beds show regular grain-size

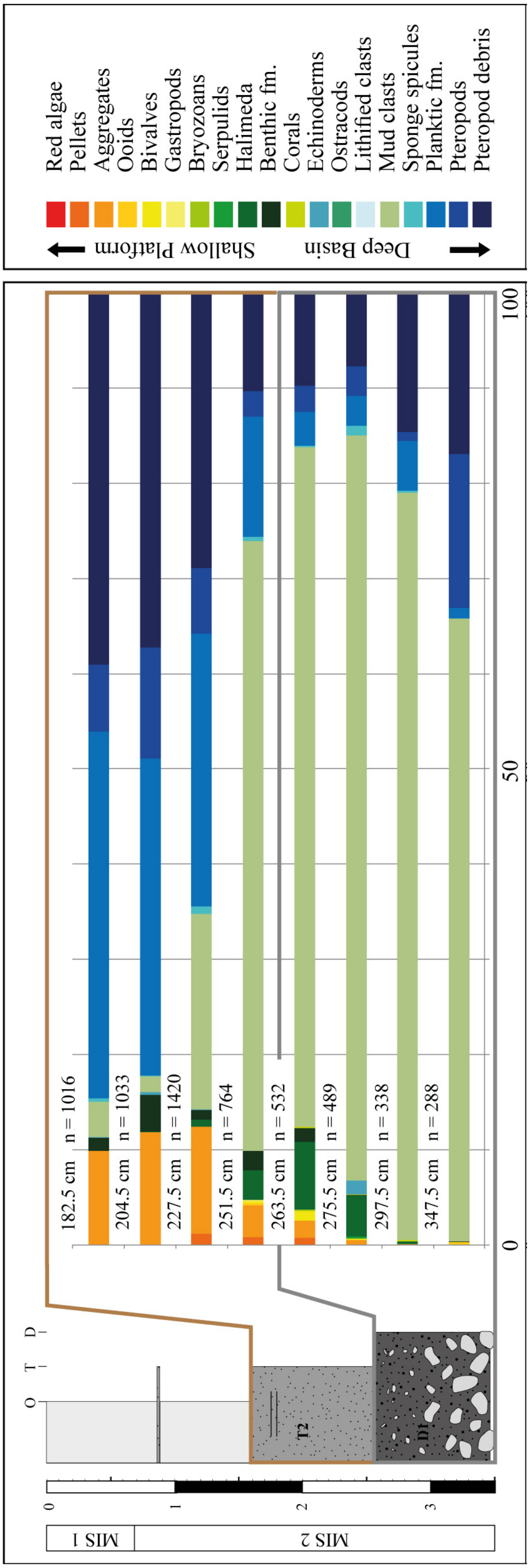


**Fig. 9.** Normalized point counting for KS26. A simplified representation of the core is shown to the left. Stratigraphic position and number of counts (n) is indicated for each sample. Primary depositional environments are intentionally vague, because species of the same group may occupy various settings.

pulses of coarse and very coarse sand-sized fractions (T31–32; T21–23; T10; Fig. 10). Mud clasts are rare, centimetre-sized and only occur in T32, T24, T18 and T10–11. Mud clasts have a pelagic signature (mainly planktic foraminifera, pteropods and mud), with a bimodal grain-size distribution rarely exceeding 150 µm.

Point counting of T-beds reveals skeletal and non-skeletal grains derived from a continuum of shallow to deep-depositional environments. From the base to the top of KS24, three assemblages are depicted from nine studied beds (Fig. 12).

**1** The first assemblage (T31 and T32) comprises significant proportions (>30%) of aggregates, *Halimeda*, and benthic foraminifera. Benthic foraminifera are dominantly shallow-water species, for example, *Archaias angulatus* (Fichtel & Moll, 1798) and *Amphistegina lessonii* to a lesser extent. The tests of many specimens show strong abrasion. *Halimeda* frequently occur in association with serpulids. Both bryozoan and coral grains are more abundant in T32 than T31.

**2** The second assemblage (T14, T20 and T23) reveals significant percentages (up to 90%) of planktic foraminifera, pteropods and associated debris. Aggregates appear in various proportions (1 to 24%) in T-beds. *Halimeda* and benthic foraminifera (*Archaias angulatus* and *Amphistegina lessonii*) are in larger proportions in T23 (*ca* 10%) than in T14 and T20 (*ca* 1 to 3%).

**3** The third assemblage (T1, T5, T8 and T10) is typified by ooids ranging from 15% (in T1) to 85% (in T8). Most of the remaining grains are planktics in variable amounts (6 to 43%) and pellets in fair proportions (3 to 10%). Benthic foraminifera identified in T1 and T10 include *Archaias angulatus*, *Archaias* var. *angulatus* and a few specimens of Miliolidae sp.

Point counting at several stratigraphic positions within T-beds determined compositional variations at the bed scale (Fig. 12). For T32, seven samples collected from base to top show varying

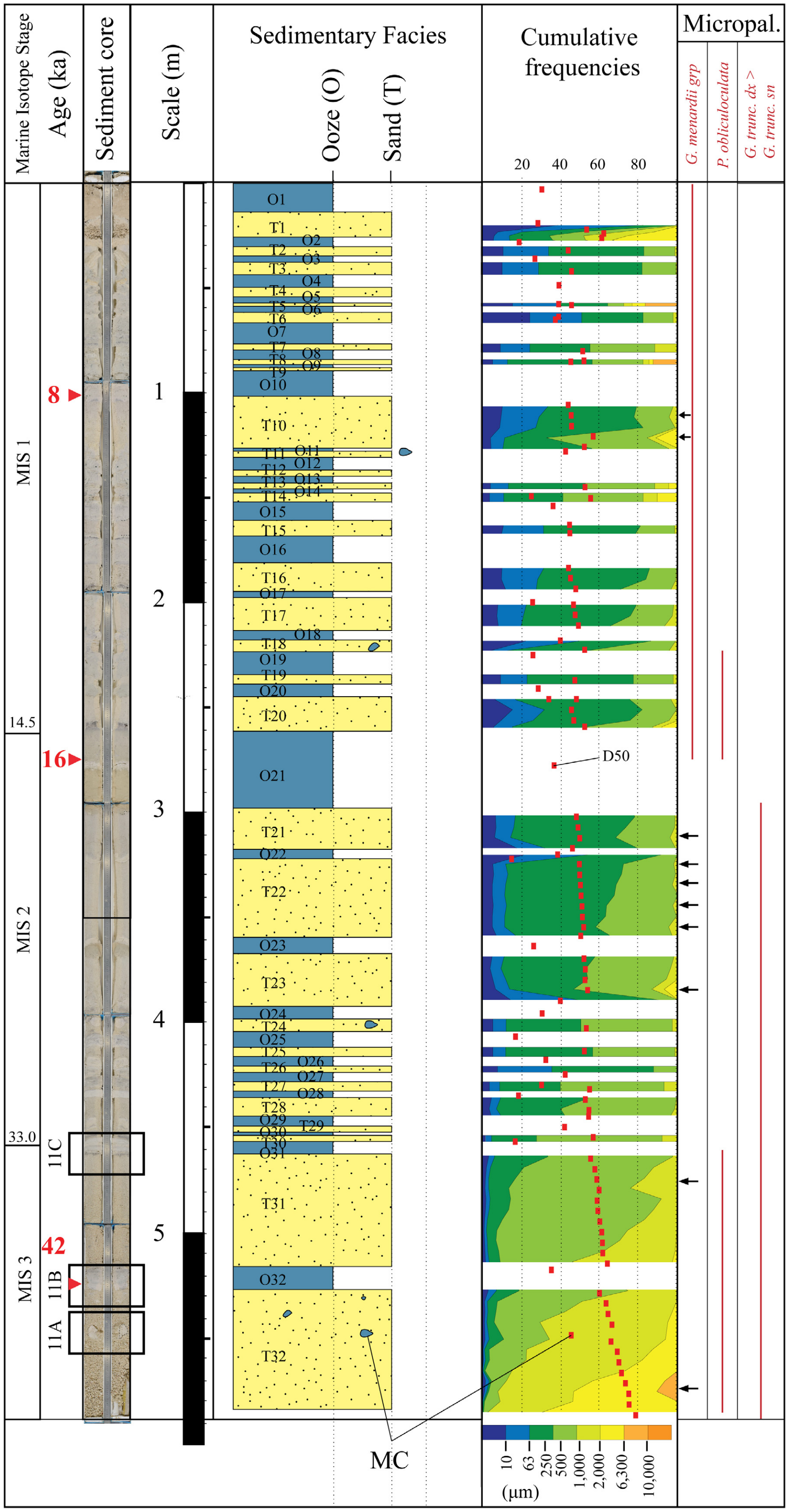


**Fig. 10.** Sediment core KS24. Left to right: proposed age model of the deposits according to biostratigraphy and radiocarbon dating (red arrows); core photograph with black boxes referring to Fig. 11, scale (in metres); simplified representation of the core with interval coding; cumulative grain-size frequencies for each sample (grain-size pulses represented with black arrows); median grain-size (D50, red squares) and micropalaeontology. MC, mud clasts. From 0 to 1 m, interval thicknesses and sedimentary features may be slightly disrupted due to coring disturbance.

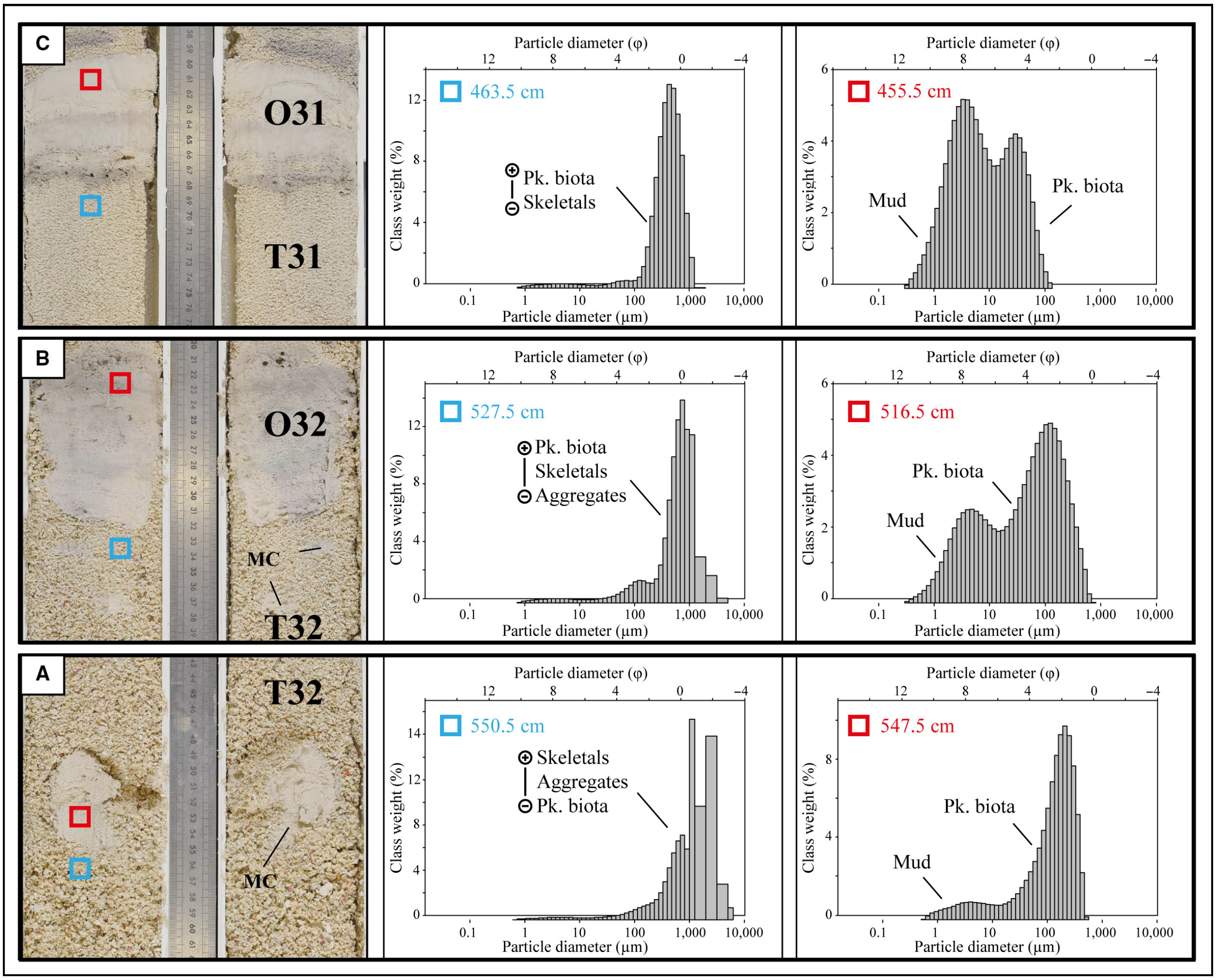


**Fig. 11.** High-resolution photographs of KS24 for stratigraphic positions shown in Fig. 10. Particle diameters and their respective percentage within the total assemblage. Blue and red squares show the location each sample. Differences between grain-size classes are inherent to the measurement method, laser or sieving. Planktic biota includes planktic foraminifera and pteropods. MC, mud clasts; Pk., planktic. The panels on the far-left hand-side are 20 cm across.

grain-type trends. The first trend corresponds to an increased fraction of pteropods and associated debris (<1% at the base and 25% at the top). The second trend shows a planktic foraminifera increase from base to top (1 to 30%). The third trend consists of a progressive increase of benthic foraminifera to the top (3 to 16%). Conversely, *Halimeda* and coral fragments decrease from 36 to 5% and 3% to zero, respectively. Similar though less pronounced decreasing upward trends are observed for bryozoans, gastropods and calcareous sponges. For T31, grains were counted at four stratigraphic positions (Fig. 12). Combined planktic fractions (i.e. foraminifera, pteropods and debris) increase from 32% at the base to 45% at the top of the bed. Conversely, percentages for *Halimeda* and serpulids, bryozoans and ooids decrease upward. T23, T14 and T1 were only sampled at two stratigraphic positions. Combined planktics show a decrease upward for T23 and T14, while T1 suggests a reverse trend. For both T23 and T14, the aggregate proportion strongly increases upward (three-fold for T23 and two-fold for T14).

The O-intervals reveal varied proportions of planktic foraminifera (for example, *Globorotalia inflata*, *Neogloboquadrina dutertrei* and *Pulleniatina obliquiloculata*) along the sedimentary

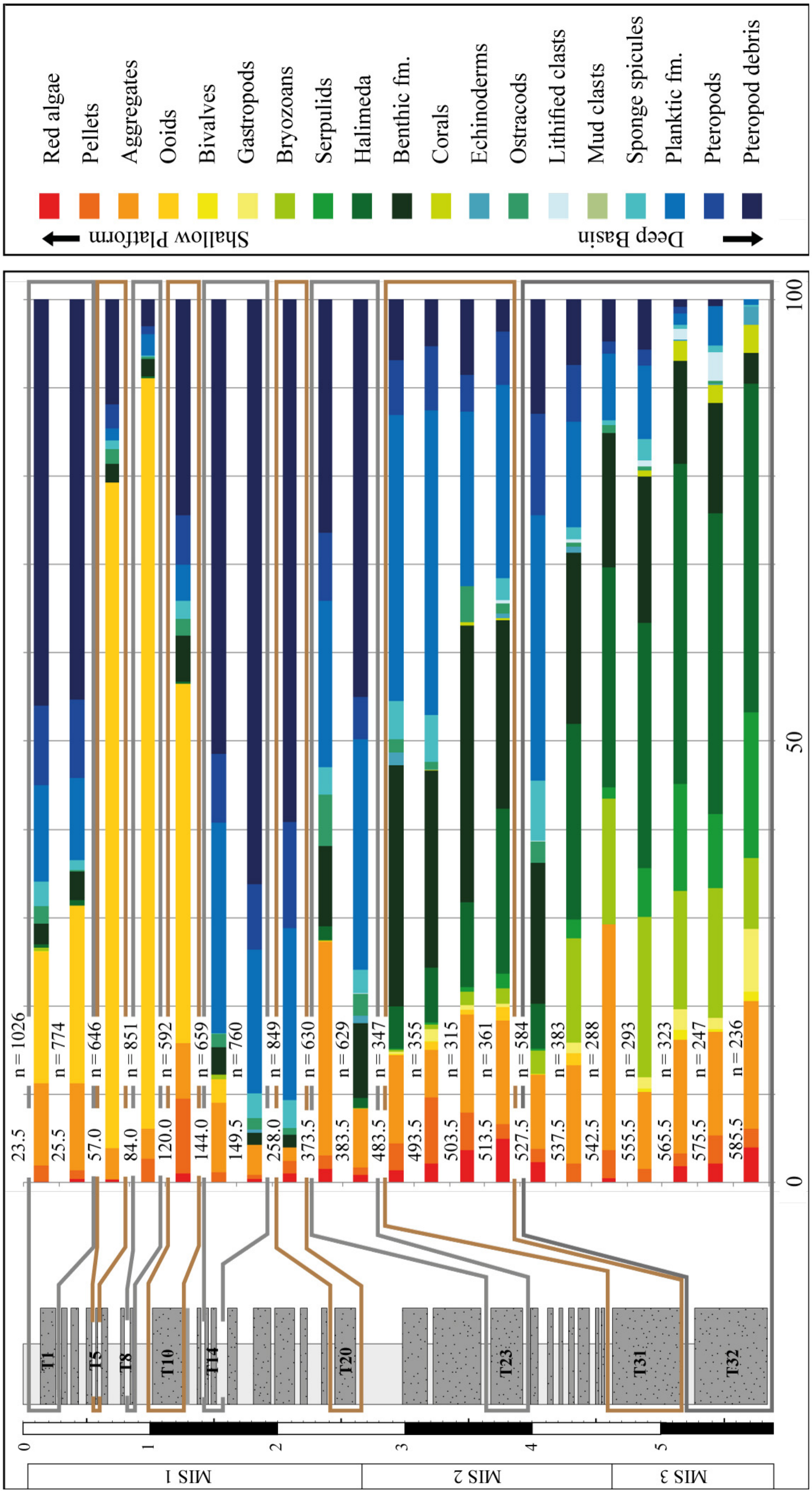


**Fig. 12.** Normalized point counting for KS24. A simplified representation of the core is shown to the left. Stratigraphic position and number of counts (n) is indicated for each sample. Primary depositional environments are intentionally vague, as species of the same group may occupy various settings.

succession. This suggests a unique pelagic signature for each stratigraphic position. O-intervals O31 to O14 reveal a planktic content (foraminifera and pteropods), that is often mixed with ostracods and sponge spicules. Only four out of 20 samples show limited quantities of shelf-derived grains (for example, *Halimeda*). In contrast, all samples collected from O10 to O1 contain shelf-derived grains (for example, pellets and ooids), often in significant proportions (30 to 50%) when compared with the planktic assemblage.

### Timing of deposition and strontium concentrations

In order to evaluate the effect of sea level on the sedimentary record of Exuma Valley, preservation rates are calculated in relation to interglacial and glacial marine isotopic stages (MIS1 to MIS3) using radiocarbon isotopes and micropalaeontology. Strontium/calcium ratios are then used as a proxy of aragonite to allow a detailed reconstruction of glacial versus interglacial periods (Counts *et al.*, 2019).

*Timing of deposition*

Core KS24 reveals sharp contacts between coarse-grained T-beds and muddy O-intervals (Fig. 10). T-beds show a shallow-water signature whereas O-intervals are predominantly characterized by a deep-water pelagic signal (Fig. 12). These characteristics point to allogenic carbonate grains quickly-emplaced in T-beds (i.e. event-beds), followed by longer periods of pelagic fall-out in O-intervals. Similar O-intervals dominated by a deep-water signal are found at the top of KS26 (O1 to O2; Fig. 7).

Radiocarbon dating performed in O-intervals yielded ages ranging from present to 37 ka for KS26 (137.5 cm) and to 42 ka for KS24 (525.0 cm; Table 3). The bases of these two cores could not be dated due to the presence of event-beds. Besides radiocarbon dating, the occurrence of *Globorotalia menardii* and the absence of *Pulleniatina obliquiloculata* were used to infer the extent of the interglacial period MIS1 and glacial period MIS3, respectively (Figs 7 and 10). MIS1 covers 210 cm in KS24 and only 65 cm in KS26. This difference in thickness is partially due to the absence of sandy event-beds in KS26 during MIS1, while many event-beds occur in KS24 (Figs 7 and 10). Moreover, the cumulative amount of carbonate ooze (i.e. when T-beds are removed) in KS24 is still two times thicker than in KS26 during MIS1. Similar observations were made for MIS2. A comparison for MIS3 could not be made due to incompleteness of the sedimentary record in both cores (Figs 7 and 10).

The interglacial MIS1 is associated with 20 event-beds in KS24 (i.e. one event each 725 years on average) while no event-bed occurred at the location of KS26 during MIS1. During glacial periods (MIS2–MIS3), 12 event-beds are recorded in KS24 (i.e. one event each 2300 years) while only two event-beds are recorded in KS26 (i.e. one event each 11 250 years). Aforementioned numbers are minimum estimates that do not consider potential bypass or erosion.

In KS24, bulk accumulation rates are similar for both the last interglacial (MIS1) and the glacial period (MIS2–MIS3; Fig. 13A). However, when distinguishing allochthonous T-beds from autochthonous O-intervals, unambiguous trends appear: first, accumulation rates of carbonate ooze in EV during MIS1 exceed those calculated for MIS2–MIS3 by 11% (Fig. 13B); second, there are three times more events reaching the seafloor of EV during interglacial MIS1 (Fig. 13C), but those accumulate less sediment (by 19%) than their glacial counterparts (i.e. MIS2–MIS3; Fig. 13D).

*Strontium concentrations*

Ratios of strontium (Sr) to calcium (Ca) derived from XRF-core scanning are plotted for KS24 in Fig. 14. There is a sharp contrast between the Sr/Ca trend in glacial (MIS2–MIS3) versus interglacial (MIS1) periods. During MIS2–MIS3, Sr/Ca are lower (average *ca* 0.10) in O-intervals compared to T-beds (average *ca* 0.16; Fig. 14). Sr/Ca ratios within T-beds are grain-size-dependent during MIS2–MIS3, i.e. the smaller the grain-size, the lower the Sr/Ca ratio (Fig. 14). In contrast, during MIS1, Sr/Ca ratios show similar values between O-intervals and T-beds, with a general increase from 250.0 to 107.0 cm followed by a decrease from 107.0 cm to the core top.

## INTERPRETATIONS AND DISCUSSION

Seafloor morphology and sediment cores covering the last *ca* 40 kyr provide an integrated archive of carbonate sediment transfer onto the submarine slopes of Exuma Valley (EV). Three diagnostic deposits are inferred from the sediment cores (Figs 7 and 10). First, the D-bed classifies as a *debrite* based on poor sorting of the reworked boulder-size clasts embedded in a

**Table 3.** Radiocarbon dating for six samples picked along the sediment cores KS26 and KS24 (Pk., planktic; Pt., pteropods).

| Core | Depth (cm) | Material | Lab code | Conventional $^{14}$C age (BP) | 2-sigma cal yr BP age ranges | Cal yr BP age median probability |
|---|---|---|---|---|---|---|
| CAR2KS26 | 7.5 | Pk. foraminifera | 519198 | 1450 ± 30 | 917–1075 | 994 |
| CAR2KS26 | 89.5 | Pk. foraminifera | 519199 | 18 230 ± 70 | 21 356–21 841 | 21 600 |
| CAR2KS26 | 137.5 | Pk. foraminifera | 519200 | 33 380 ± 210 | 36 375–37 885 | 37 047 |
| CAR2KS24 | 102.5 | Pk. foraminifera & Pt. | 519201 | 7990 ± 30 | 8375–8527 | 8443 |
| CAR2KS24 | 276.5 | Pk. foraminifera | 519202 | 13 450 ± 40 | 15 376–15 821 | 15 635 |
| CAR2KS24 | 525.0 | Pk. foraminifera | 519203 | 38 260 ± 350 | 41 637–42 630 | 42 140 |

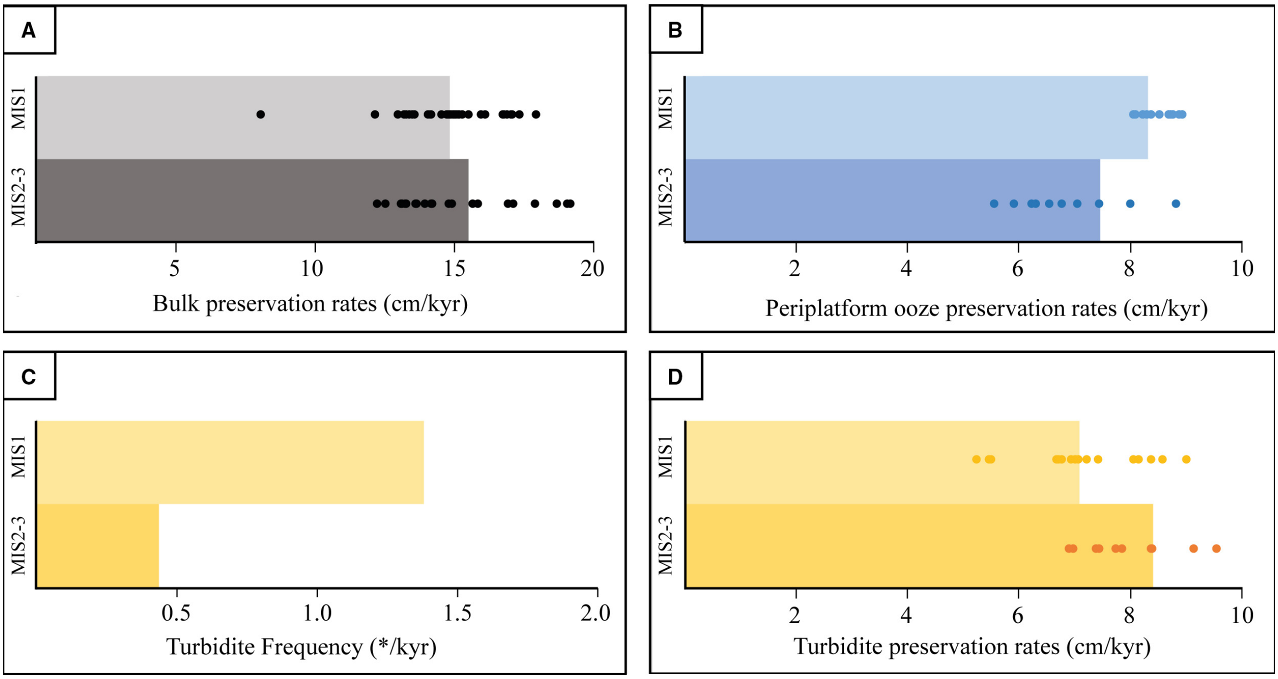


**Fig. 13.** Accumulation rates calculated for KS24. Calculation for each interval (dots) are averaged on each time period (bands): (A) bulk accumulation rate; (B) peri-platform ooze accumulation rate; (C) turbidite frequency; and (D) turbidite accumulation rate.

sandy matrix (Fig. 8A). Frictional freezing and '*en masse*' deposition by a debris flow are proposed for the settling of this debrite (Mulder & Alexander, 2001b). Second, sandy T-beds classify as *turbidites* owing to the presence of: (i) abraded allochems (for example, *Halimeda* flakes and shallow-water benthic foraminifera); (ii) a fining-upward trend (Fig. 10); (iii) horizontal parallel laminations (Fig. 8C); and (iv) erosional features (for example, mud clasts interpreted as rip-up clasts; Fig. 11A). These characteristics point to incremental deposition and occasional seafloor erosion by turbidity currents (Kuenen & Migliorini, 1950; Bouma, 1962). Third, carbonate ooze (O-intervals) classifies as *background* and *peri-platform* deposits due to: (i) their fine-grained (D50 = 5 to 120 µm; Figs 7 and 10), planktic-dominated composition; (ii) their sharp contacts (in grain size and colour) with T-beds; and (iii) the absence of flow indices such as sorting or laminations (Bornhold & Pilkey, 1971). Based on this classification, the following sections aim at linking: (i) seafloor morphology and depositional processes; (ii) sorting mechanisms in event-beds; and (iii) sea-level variations and sediment export.

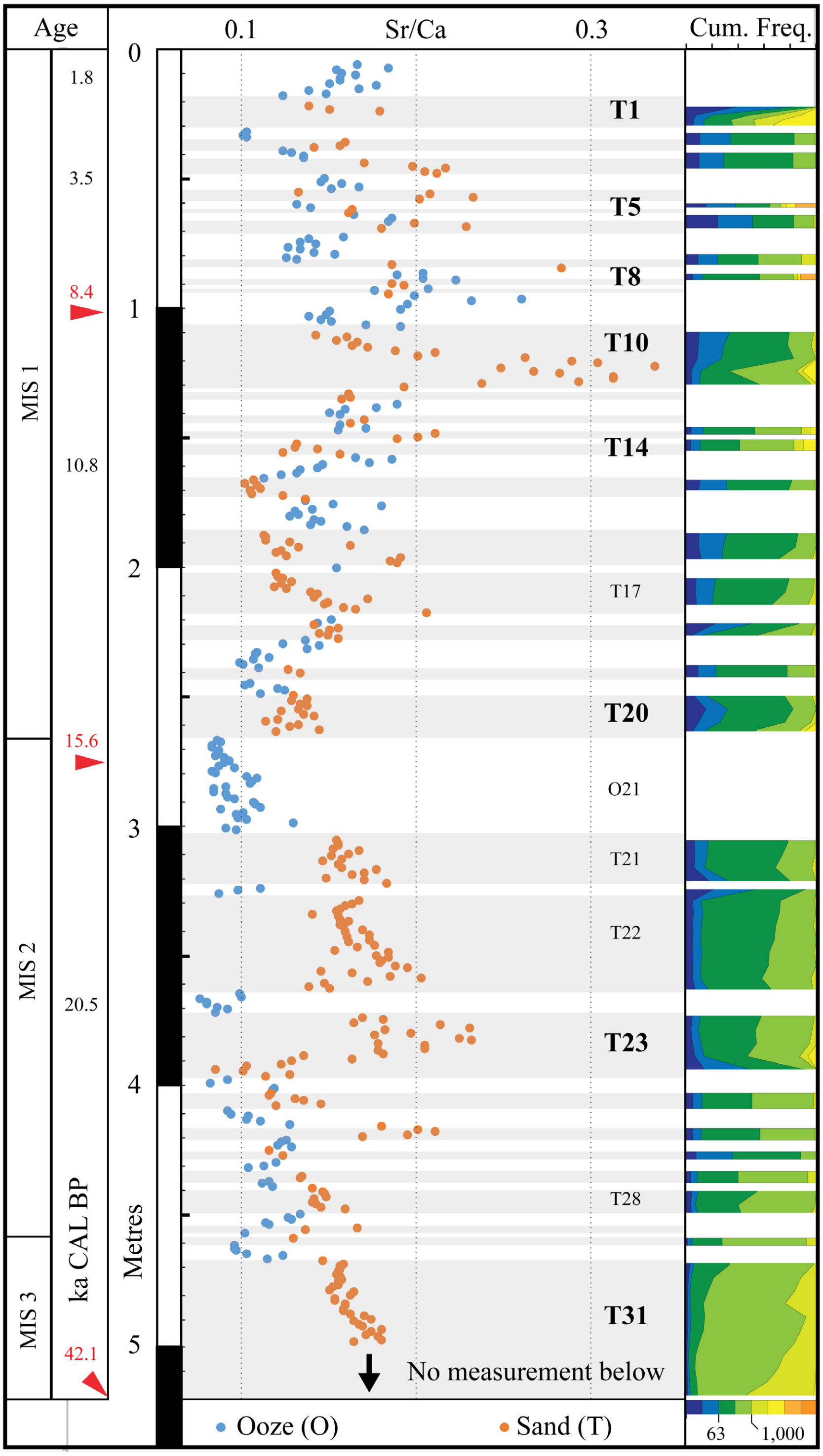


**Fig. 14.** Strontium to calcium ratios for KS24 derived from the XRF core logger. From left to right: age model of the deposits with Marine Isotope Stages (MIS), time-constraints from radiocarbon dating (red) and calculated ages (black), scale in metres, Sr/Ca ratios for O-intervals (blue) and T-beds (orange), name for some T-beds (bold for those presented in Fig. 12) and cumulative grain-size frequencies.

## Knickpoints and depositional products

### *Origin of knickpoints*

Knickpoints can be formed by litho-structural contrasts (Mulder *et al.*, 2018, 2019), hydrodynamic processes (Toniolo & Cantelli, 2007) or a combination of both. Three processes are proposed for Exuma Valley (EV) based on morphological and deposit-based observations (Figs 3, 4 and 5). First, *slope-collapse* of the active valley-flank is proposed for knickpoint K1, because of the oblique orientation of the knickpoint lip with respect to the valley axis. K1 shares morphometric similarities with slope collapses on the surrounding flanks in Exuma Sound (for example, kilometre-scale extension of the headwall scarps; Figs 3 and 4A). Second, *flow relaxation* is defined as the rapid expansion of a turbidity current leaving a confinement, inducing seafloor erosion by increased turbulence and basal shearing (Gray *et al.*, 2005; Hofstra *et al.*, 2015; Pohl *et al.*, 2019). This mechanism is proposed for the inception of K2, based on the narrowing and subsequent enlargement of the valley at the K2 location (Figs 2C and 4B). Additionally, K2 shows a crescentic lip and a spoon-shaped lower slope. Similar crescentic, spoon-shaped scours (up to 2.5 km wide and 20 m deep) were observed in channel–levée transition zones elsewhere (Wynn *et al.*, 2002). Third, *erosional side gullies* prolonging into the main axis of EV are inferred for the initiation of K3, K4 and K5 (Fig. 4A and C). These side gullies flank the slopes of Conception and Long Island (Fig. 1). Similar relations between lateral gullies and knickpoints inception were proposed in section 3 of EV for K6 (Fig. 2; Mulder *et al.*, 2019). The offset of K4 and K5 with their respective gully axis likely relates to the upstream-migration of the knickpoint lip that was attributed to a hydraulic jump in other sedimentary systems (Fig. 4A; Zhang *et al.*, 2019; Slootman & Cartigny, 2020).

### *Deposits in section 1 (Knickpoint K1, core KS26)*

Core KS26 is located within a depression 0.3 km downstream of K1 and composed of a debrite (D1), turbidites (T2 and T1) and two carbonate ooze intervals (O2 and O1; Figs 6A and 7). Both poor sorting and planktic content in D1 suggest a relatively short sediment transport distance, likely related to slope collapse at/or adjacent to K1 (Figs 4 and 6A). Mud clasts in D1 and T2 (Figs 7 and 9) are provided by the mud-dominated submarine slopes in the South of Exuma Sound (ES) (Droxler *et al.*, 1988; Reymer *et al.*, 1988; Rendle-Bühring & Reijmer, 2005). Slumps, debrites and turbidites were interpreted as the products of margin and slope collapses for the Plio-Pleistocene deposits in this area (Austin *et al.*, 1986a, 1986b, 1986c; Reymer *et al.*, 1988; Reijmer *et al.*, 1992, 2012). Scars on the seafloor also support the occurrence of slope collapses and associated deposits (see Fig. 3; Fabregas *et al.*, 2018; Mulder *et al.*, 2019). Similar deposits such as slumps, debrites or thick shale-clast lag deposits were associated with an incising channel initiation stage in siliciclastic systems (Posamentier & Kolla, 2003; Mayall *et al.*, 2006; Fildani *et al.*, 2013; Hubbard *et al.*, 2014; Bell *et al.*, 2018). The slope features and deposits observed in EV section 1 could agree with an upstream, retrogradational incision of the main axis into ES (i.e. initiation stage; Fig. 2). Additional bathymetric and core data in ES are needed to fully constrain this process.

### Deposits in section 2 (Knickpoint K5, core KS24)

In EV section 2, knickpoints consist of slope breaks followed by topographic highs (K2 to K5; Fig. 15A): K5 shows upstream-dipping beds (Fig. 6B) of alternating sand-mud facies (Figs 10 and 15B). These slope breaks and upstream-dipping beds suggest an erosional versus depositional character of density flows (Fig. 5). Field and experimental studies related this alternating behaviour to Froude supercritical flows (over the knickpoint face) transitioning into subcritical flows (at the lower slope break) through a hydraulic jump (Komar, 1971; Postma & Cartigny, 2014). Erosion of the steep face followed by deposition on the lower slope results in upstream bedform migration (Parker & Izumi, 2000; Cartigny *et al.*, 2011; Hughes Clarke, 2016; Slootman & Cartigny, 2020), which is expressed in EV at the lower slope-break of knickpoints K2 to K5. It is proposed that turbidites in KS24 (Fig. 10) are the depositional expression of episodic subcritical flows downstream of knickpoint K5 (Fig. 15C). Hence, the oldest coarse and thick turbidites would result from high-density flows close to the hydraulic jump (for example, T31 and T32; Figs 10 and 15C; Postma & Cartigny, 2014). Conversely, younger event-beds would reflect lower density flows settling away from the hydraulic jump (for example, T10 to T1; Figs 10 and 15C; Postma & Cartigny, 2014). Carbonate ooze intervals in KS24 are interpreted as longer periods of hemipelagic sedimentation between events (Fig. 11). Long-wavelength bedforms such as those interpreted in EV (i.e. >1 km) are challenging to recognize in cores and outcrops due to the difficulty in reconstructing depositional angles. Thinning and fining-upward beds are often interpreted as channel filling-up sequences in outcrops (Hubbard *et al.*, 2014; Covault *et al.*, 2016; Bell *et al.*, 2018). Integrated bathymetry and sediment cores proposed here allows to refine recognition of such sequences in the depositional record.

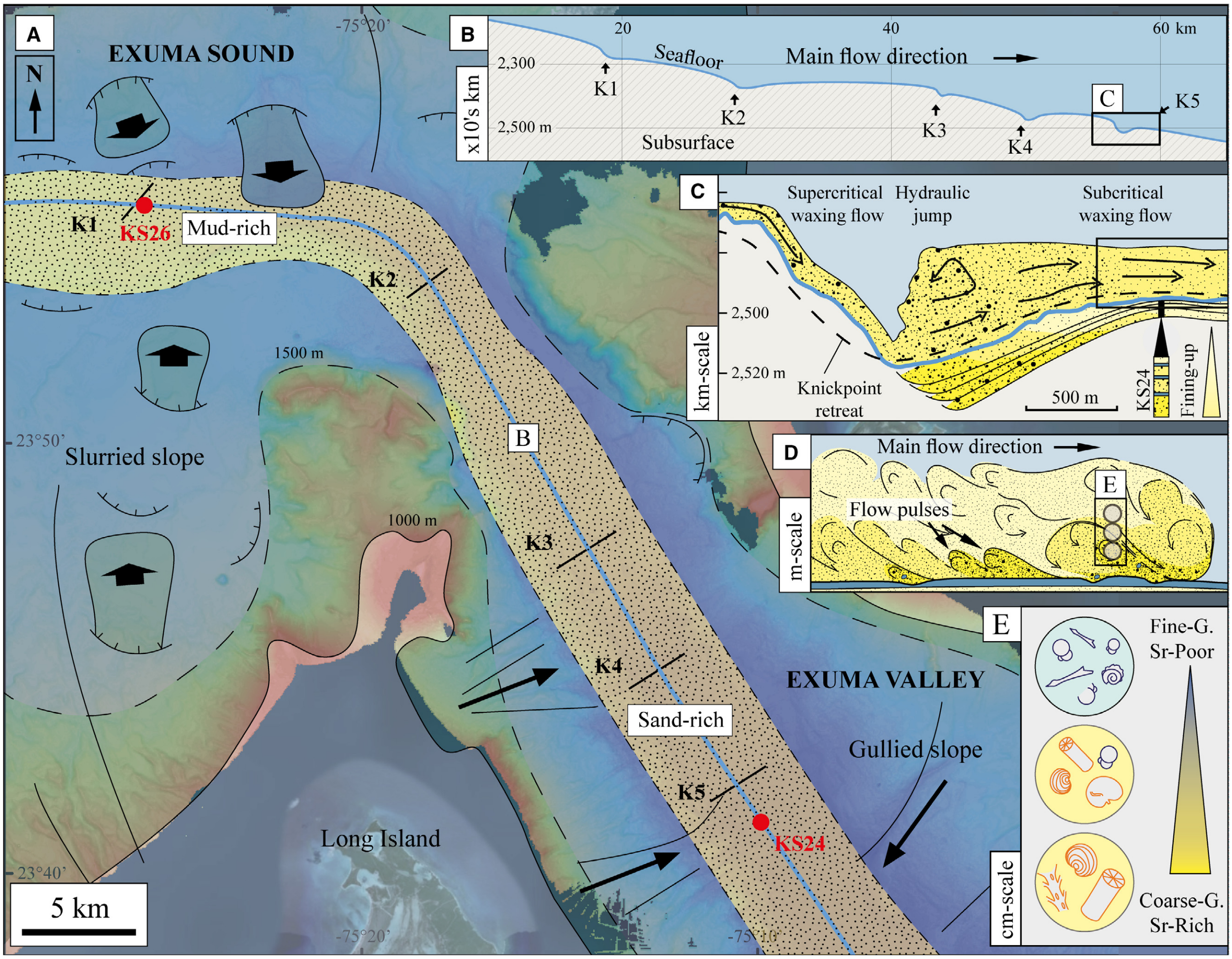


**Fig. 15.** Integrated scales of observation of deep-water processes and products in Exuma Valley. (A) Schematic representation of the morphological attributes of the study area. (B) Simplified slope profile of Exuma Valley derived from Fig. 5A and knickpoint location (tens of kilometres). (C) Real seafloor profile of K5 with scaled sediment core KS24 combined with an interpreted sequence of deposits and density flow (kilometre-scale). (D) Hypothetical density flow showing in-flow grain-size segregation and flow-pulses. (E) Representative biogenic grains and grain-size sorting within a density flow governing strontium concentration within turbidites (orange colour reflects a shallow-water origin, blue colour reflects a deep-water origin).

## Sorting mechanisms in event-beds

The debrite–turbidite couplet in KS26 is considered as the product of a single hybrid event flow (D1–T2; Figs 7 and 8). Debrite–turbidite couplets, also called hybrid event-beds, are reported from modern (Crevello & Schlager, 1980; Haughton *et al.*, 2003; Talling *et al.*, 2004) and ancient submarine environments (Kleverlaan, 1987; Labaume *et al.*, 1987; Haughton *et al.*, 2009; Fallgatter *et al.*, 2017). Vertical partitioning of debrite–turbidite couplets was shown to result from coexisting mechanisms within a single density flow (Hampton, 1972; Krause & Oldershaw, 1979). Experiments by Hampton (1972) point to sediment ejection from the snout of the debris flow at the base and concomitant incorporation into an overlying, dilute turbulent cloud at the top. The end-product was identified in lower Cambrian rocks (Krause & Oldershaw, 1979) and in Pleistocene deposits of ES (Crevello & Schlager, 1980). Sedimentary features supporting the hybrid-bed interpretation in KS26 include: (i) the poorly-sorted outsized mud clasts in debrite D1 grading upward into a clean sandy turbidite T2 (Fig. 7); (ii) grain types with similar sources; and (iii) a vertical sorting of grain type proportions throughout the bed

(Fig. 9). A general fining-upward trend in T2 records the waning phase of the turbidity current. Deviations of the general fining-upward trend (i.e. grain-size pulses; Fig. 7) suggest internal flow-pulses formed by successive trains of billows related to flow unsteadiness (Fig. 15D; Kelvin-Helmholtz instabilities; Simpson, 1969; Kneller & Buckee, 2000).

Grain sorting at the bed scale is now discussed for event-beds observed in KS26 and KS24. Grain sorting is controlled by the *size*, *density* and *shape* of individual grains (Maiklem, 1968; Braithwaite, 1973; Herbig & Mamet, 1994; Ferguson & Church, 2004; Hodson & Alexander, 2010; de Boer *et al.*, 2018; Reijmer *et al.*, 2019; Slootman *et al.*, 2019). *Size-control* is evidenced in the hybrid event-bed (D1–T2; KS26) by the predominance of mud clasts at the base of the deposit, while planktic biota become more abundant towards the top (Fig. 9). Mud clasts may cover much larger grain-size ranges as opposed to small (<500 μm) skeletal organisms such as pteropods or planktic foraminifera. The latter are thus logically more abundant in the upper, smaller grain-size fractions of the turbidite. A similar reasoning explains the increasing upward planktic proportions in the turbidites T31 and T32 (KS24; Fig. 12), where very coarse and pebble-size sand fractions are dominant at the base. *Density control* is demonstrated by the mud clast versus aggregate proportions in the D1–T2 couplet for similar grain sizes. The interval revealed an increasing proportion of porous aggregates upward at the expense of tight mud clasts (Fig. 9). *Grain-shape control* on the sorting of carbonate grains is difficult to quantify in this dataset, although the variations in grain shapes of individual components (for example, conical pteropods versus globular planktic foraminifera) offer further research perspectives (Caromel *et al.*, 2014).

Grain-size sorting in turbidites is strongly correlated with Sr/Ca variations at the bed-scale, i.e. the coarser the grain size, the higher Sr/Ca ratio (see T31 and T23–T21 in KS24; Fig. 14). Coarsest grain-size fractions are dominated by shallow-water, strontium-rich skeletal debris (for example, *Halimeda*), while the upper, finer part is increasingly composed of planktic, strontium-depleted organisms (Fig. 15D and E).

## Sea-level variations and carbonate export

The sediment record in EV is controlled by seafloor morphology and grain sources (see *Results* section). In this section, climatic control on the Bahamian carbonate system is discussed using the 40 kyr long record preserved in KS26 and KS24. First, event-bed frequency is discussed in relation to glacial–interglacial cycles and hurricanes. Second, inundation stages (i.e. *emersion and re-flooding*) of shallow-water banks induced by glacial–interglacial cycles are discussed.

### *Event-bed frequency*

Climate-induced changes (for example, sea level) and extreme events (for example, hurricanes) control carbonate production and export (Hine *et al.*, 1981; Kendall & Schlager, 1981; Droxler & Schlager, 1985; Roth & Reijmer, 2004, 2005). For example, glacial periods were responsible for sea-level falls of 80 to 150 m in the Bahamas during the Quaternary, decreasing carbonate export and density-flow event frequency (Fairbanks & Matthews, 1978; Boardman *et al.*, 1988; Haak & Schlager, 1989).

Previous studies derived turbidite frequencies from sediment cores in different locations of the Bahamas (Fig. 1A).

**1** In the Columbus Basin, one event was recorded every 3 to 6 kyr during the last *ca* 25 kyr (Bornhold & Pilkey, 1971).

**2** In the Tongue of the Ocean (TOTO), estimations vary from 0.5 to 10 kyr depending on the sub-basin location (Rusnak & Nesteroff, 1964). Turbidites were further shown to occur more frequently (i.e. up to 14 times) in interglacial than in glacial periods (Droxler & Schlager, 1985).

**3** In ES, the frequency of flows reaching the basin floor is about one every 10 to 13 kyr during the last *ca* 120 kyr (Crevello & Schlager, 1980). In this study, flow frequency calculated for KS26 (i.e. one every 11 kyr) confirms those previously reported in ES (Crevello & Schlager, 1980).

**4** For the first time, flow frequencies are shown in EV (KS24), where interglacial turbidites are three times more frequent than the glacial ones (i.e. 1 event each 725 years versus 1 event each 2300 years, respectively; Fig. 13C). However, interglacial turbidites are thinner (i.e. lower preservation potential) than the glacial ones. (Fig. 13D). Seafloor erosion associated with knickpoint upstream migration is suggested to explain the changes of accumulation potential downstream of K5 (Fig. 15C).

Besides sea-level changes, hurricanes that frequently strike the platform top are thought to modulate off-bank shedding (Pilskaln *et al.*, 1989;

 

Rankey *et al.*, 2004; Toomey *et al.*, 2013). Turbidite frequency estimated in this study appears much lower compared to previous estimates for hurricane frequency in the Bahamas (i.e. eight to ten hurricanes every ten years; Pilskaln *et al.*, 1989). It is hypothesized that hurricanes can produce either powerful, long run-out density flows (recorded by the turbidites in KS24 for example) or smaller flows (Reeder & Rankey, 2009) that are not/poorly expressed in the cores.

### *Emersion of shallow-water banks during MIS2–MIS3*

*Emersion* and subaerial exposure of the GBB prevailed from the end of the last interglacial (MIS5e, 120 ka) up to the onset of the Holocene flooding during MIS1 (*ca* 7.6 ka; Fairbanks & Matthews, 1978; Boardman *et al.*, 1988; Haak & Schlager, 1989; Roth & Reijmer, 2004; Fauquembergue *et al.*, 2018). Skeletal-dominated grains are observed in turbidites of KS24 during this period (for example, *Halimeda*, bryozoans and corals; Fig. 12). Skeletal particles (Sr-rich) were produced by coralgal belts and possibly seagrass meadows which were relocated along the fringe of carbonate banks following sea-level fall (Purdy, 1963; Enos, 1974; Haak & Schlager, 1989; Grammer & Ginsburg, 1992; Reijmer *et al.*, 2009). At the same time, the mud dominated platform tops (also Sr-rich) and oolitic shoal complexes were switched off. A strong contrast between Sr-rich turbidites and Sr-poor ooze intervals suggests that ooze intervals originate from pelagic fall-out (Fig. 14). Sea-level falls have also been invoked to create slope instabilities, favouring a release of pore-water overpressure (Spence & Tucker, 1997) which could explain the triggering of the D1–T2 (KS26) and its exclusive deep-water assemblage (Fig. 9).

### *Re-flooding of shallow-water banks during Marine Isotope Stage 1*

*Re-flooding* of shallow-water banks in the Bahamas was inferred to meltwater pulses 1A, 1B and 1C (MWP; *ca* 14.6 ka, 11.5 ka and 9.5 ka, respectively; Mullins *et al.*, 1984; Roth & Reijmer, 2004, 2005; Fauquembergue *et al.*, 2018). These pulses are major triggers of the sea-level rise acceleration worldwide (Liu & Milliman, 2004; Lambeck *et al.*, 2011; Deschamps *et al.*, 2012). Off the Little Bahama Bank, these events are recorded by carbonate 'terraces', feeding a peri-platform wedge (Rankey & Doolittle, 2012; Mulder *et al.*, 2017; Fauquembergue *et al.*, 2018). The flooding initiation of carbonate banks surrounding Northwest Providence Channel is estimated at 6.0 ka (Pilskaln *et al.*, 1989) and *ca* 7.6 ka on the GBB (Fig. 1A; Wilber *et al.*, 1990; Roth & Reijmer, 2004). In EV, a progressive input of Sr-rich fine-grained particles at *ca* 14.5 ka (Fig. 14) matches with the meltwater pulse 1A. The presence of re-sedimented ooids at *ca* 10 ka (Fig. 14) reflects the activation of the ooid shoal complexes when the outer shelf was re-flooded (Rankey & Reeder, 2011). The maximum input of Sr-rich particles in turbidites can be correlated with the ooid peak at *ca* 8.4 ka (Figs 12 and 14).

The maximum flooding is reached around 4.0 or 5.0 ka in the Bahamas and corresponds to a complete inundation of the carbonate banks massively exporting aragonite needles (Hine *et al.*, 1981; Roth & Reijmer, 2004; Fauquembergue *et al.*, 2018). Density cascading triggered by the passage of cold fronts over carbonate shelves (McCave, 1972; Wilson & Roberts, 1992, 1995) could explain the export of aragonite, Sr-rich material to EV (Figs 10 and 14). This is attested to by the mixed planktic (i.e. deep) and shelf-derived signature of the carbonate ooze in the studied cores during MIS1.

## CONCLUSIONS

Exuma Valley is a huge (130 km long, 5 km wide) sediment conduit linking Exuma Sound to the Atlantic Ocean floor in the Bahamas. Integration of seafloor imaging (bathymetry and seismic) and sediment core analysis (point counting and geochemical signatures) provides a 40 kyr sedimentary record of a 60 km long transect in Exuma Valley. Seafloor morphology, flow dynamics and sea-level influence depositional processes and products in carbonate systems, as illustrated in Exuma Valley.

**1** *Knickpoints and their depositional products*: Knickpoints (i.e. upstream-migrating slope breaks) in Exuma Valley are related to surrounding morphology (for example, bank collapse and lateral gullies) and/or shaped by turbidity currents in the valley axis. Knickpoint deposits generated by bank collapse reveal a debrite–turbidite couplet with abundant mud clasts. In contrast, knickpoint deposits in the valley axis consist of numerous thinning and fining-upward sandy turbidites.

**2** *Grain sorting in carbonate gravity flows*: Each turbidite showed a vertical sorting of grain type proportions (for example, skeletal planktics at the top of the bed, mud clasts at the base), suggesting hydrodynamic sorting of carbonate grains in turbidity currents. Hydrodynamic sorting in sandy turbidites produces geochemical contrasts (strontium/calcium ratio) within event-beds that can be used to infer sediment sources: fine-grained deep-water particles (strontium-poor) rest on coarse-grained shallow-water particles (strontium-rich).

**3** *Effect of sea level on carbonate production and export*: Three times more turbidites occur during interglacial (marine isotopic stage 1) than glacial (for example, marine isotopic stages 2 and 3) periods in Exuma Valley at *ca* 2500 m water depth. Grain composition and geochemical signatures allow for a reconstruction of climate-driven emersion, re-flooding and highstand shedding of shallow-water banks for the last *ca* 40 kyr. During glacial intervals, coralgal belts located on the rimming slopes of Long and Conception islands nourished Exuma Valley. In contrast, the progressive re-flooding of shallow-water banks during the latest interglacial favoured the offbank export of carbonate mud and sands (for example, ooid-rich turbidites).

The sedimentary record of modern deep-water carbonate systems can be unravelled by linking seafloor morphology and resulting deposits. This integrated approach helps to refine understanding of the production, transfer and preservation of carbonate sediments from source to sink.

## ACKNOWLEDGEMENTS

The Captain and crew of *R/V L'Atalante* are thanked for their craftmanship during the Carambar 2 Cruise. KFUPM-CPG is thanked for financial support. Technical support of the core lab in Bordeaux by P. Lebleu, I. Billy and O. Ther is much appreciated. Prof. Kaminski (KFUPM-CPG) is thanked for discussions on benthic foraminifera. J. Niard (Bordeaux University) is acknowledged for his involvement in the grain-size analyses, and K. Fauquembergue (Bordeaux) for MSCL data acquisition. Post-docs A. Slootman, A. Hairabian and J. Jaballah of the Carbonate Sedimentology Group at the College of Petroleum Engineering & Geosciences (CSG@CPG) as well as visiting PhD student V. Randazzo (Palermo University) are thanked for their support and fruitful discussions. Editor-in-Chief Peir Pufahl, Associate Editor Tracy Frank and two reviewers; Irene Cornacchia and an anonymous reviewer are thanked for their helpful comments and reviews. This is CSG&CPG contribution no. 46.

## CONFLICT OF INTEREST

The authors declare no conflict of interest.

## DATA AVAILABILITY STATEMENT

The data that support the findings of this study are available on request from the corresponding author. The data are not publicly available due to privacy or ethical restrictions.

## REFERENCES

**Anselmetti, F.S.** and **Eberli, G.P.** (1993) Controls on sonic velocity in carbonates. *Pure Appl. Geophys.*, **141**, 287–293.

**Austin, J.A.**, **Schlager, W.**, **Palmer, A.A.**, et al. (1986a) *Site 631: Exuma Sound. Proceedings Initial Reports*, ODP, 101. College Station, TX, 341–386.

**Austin, J.A.**, **Schlager, W.**, **Palmer, A.A.**, et al. (1986b) *Site 632: Exuma Sound. Proceedings Initial Reports*, ODP, 101. College Station, TX, 387–437.

**Austin, J.A.**, **Schlager, W.**, **Palmer, A.A.**, et al. (1986c) *Site 633: Exuma Sound. Proceedings Initial Reports*, ODP, 101. College Station, TX, 439–482.

**Ball, M.M.**, **Harrison, C.G.A.**, **Hurley, R.J.** and **Leist, C.E.** (1969) Bathymetry in the vicinity of the Northeastern scarp of the Great Bahama Bank and Exuma Sound. *Bull. Mar. Sci.*, **19**, 243–252.

**Bell, D.**, **Kane, I.A.**, **Pontén, A.S.M.**, **Flint, S.S.**, **Hodgson, D.M.** and **Barrett, B.J.** (2018) Spatial variability in depositional reservoir quality of deep-water channel-fill and lobe deposits. *Mar. Petrol. Geol.*, **98**, 97–115.

**Boardman, M.R.**, **Dulin, L.A.** and **Kenter, R.J.** (1984) Episodes of banktop growth recorded in periplatform sediments and the chronology of Late Quaternary fluctuations in sea level. *2nd Symposium on the Geology of the Bahamas*, 128–152.

**Boardman, M.R.** and **Neumann, A.C.** (1984) Sources of periplatform carbonates: Northwest Providence Channel, Bahamas. *J. Sed. Petrol.*, **54**, 1110–1123.

**Boardman, M.R.**, **Neumann, A.C.** and **Rasmussen, K.A.** (1988) Holocene sea level in the Bahamas. *Proceedings of the Fourth Symposium on the Geology of the Bahamas*, 43–52.

**Bornhold, B.D.** and **Pilkey, O.H.** (1971) Bioclastic turbidite sedimentation in Columbus Basin, Bahamas. *Geol. Soc. Am. Bull.*, **82**, 1341–1354.

**Bosellini, A.**, **Neri, C.** and **Luciani, V.** (1993) Platform margin collapses and sequence stratigraphic organization of carbonate slopes: Cretaceous-Eocene, Gargano Promontory, southern Italy. *Terra Nova*, **5**, 282–297.

**Bouma, A.H.** (1962) *Sedimentology of some Flysch deposits; a graphic approach to facies interpretation*. Elsevier Pub. Co., Amsterdam; New York, 168 p.

**Brady, H.B.** (1877) Supplementary note on the foraminifera of the Chalk (?) of the New Britain group. *Geol. Mag.*, **4**, 534–536.

**Braithwaite, C.J.R.** (1973) Settling behaviour related to sieve analysis of skeletal sands and hyaline types. *Sedimentology*, **20**, 251–262.

**Caromel, A.G.M.**, **Schmidt, D.N.**, **Phillips, J.C.** and **Rayfield, E.J.** (2014) Hydrodynamic constraints on the evolution and ecology of planktic foraminifera. *Mar. Micropaleontol.*, **106**, 69–78.

**Cartigny, M.J.B.**, **Postma, G.**, **van den Berg, J.H.** and **Mastbergen, D.R.** (2011) A comparative study of sediment waves and cyclic steps based on geometries, internal structures and numerical modeling. *Mar. Geol.*, **280**, 40–56.

**Chabaud, L.** (2016) Modèle stratigraphique et processus sédimentaires au Quaternaire sur deux pentes carbonatées des Bahamas (leeward et windward). PhD Thesis, Université de Bordeaux, 404 pp.

**Chabaud, L.**, **Ducassou, E.**, **Tournadour, E.**, **Mulder, T.**, **Reijmer, J.J.G.**, **Conesa, G.**, **Giraudeau, J.**, **Hanquiez, V.**, **Borgomano, J.** and **Ross, L.** (2016) Sedimentary processes determining the modern carbonate periplatform drift of Little Bahama Bank. *Mar. Geol.*, **378**, 213–229.

**Cook, H.E.** and **Egbert, R.M.** (1981) Carbonate submarine fan facies along the Paleozoic prograding continental margin, western United States. *AAPG Bull.*, **65**, 913.

**Cook, H.E.**, **McDaniel, P.N.**, **Mountjoy, E.W.** and **Pray, L.C.** (1972) Allochtonous carbonate debris flows at Devonian bank (' "Reef"') margins. *Bull. Can. Petrol. Geol.*, **20**, 439–486.

**Counts, J.W.**, **Jorry, S.J.**, **Leroux, E.**, **Miramontes, E.** and **Jouet, G.** (2018) Sedimentation adjacent to atolls and volcano-cored carbonate platforms in the Mozambique Channel (SW Indian Ocean). *Mar. Geol.*, **404**, 41–59.

**Counts, J.W.**, **Jorry, S.J.**, **Vasquez Rivieros, N.**, **Jouet, G.**, **Giraudeau, J.**, **Cheron, S.**, **Boissier, A.** and **Miramontes, E.** (2019) A Late Quaternary record of highstand shedding from an isolated carbonate platform (Juan de Nova, southern Indian Ocean). *Deposit. Rec.*, **5**, 540–557.

**Covault, J.**, **Sylvester, Z.**, **Hubbard, S.**, **Jobe, Z.** and **Sech, R.** (2016) The stratigraphic record of submarine-channel evolution. *Sedimentary Record*, **14**, 4–11.

**Crevello, P.D.** and **Schlager, W.** (1980) Carbonate debris sheets and turbidites, Exuma Sound, Bahamas. *J. Sed. Petrol.*, **50**, 1121–1148.

**de Boer, R.**, **Kranenburg, J.** and **de Kruijf, M.** (2018) GECANEX – Generating calciturbidites in analogue experiments. Unpublished MSc thesis, Vrije Universiteit, Amsterdam, The Netherlands, 324 pp.

**Deschamps, P.**, **Durand, N.**, **Bard, E.**, **Hamelin, B.**, **Camoin, G.**, **Thomas, A.L.**, **Henderson, G.M.**, **Okuno, J.** and **Yokoyama, Y.** (2012) Ice-sheet collapse and sea-level rise at the Bølling warming 14,600 years ago. *Nature*, **483**, 559–564.

**Dinis, P.** and **Castilho, A.** (2012) Integrating sieving and laser data to obtain bulk grain-size distributions. *J. Sed. Res.*, **82**, 747–754.

**Droxler, A.W.** and **Schlager, W.** (1985) Glacial versus interglacial sedimentation rates and turbidite frequency in the Bahamas. *Geology*, **13**, 799–802.

**Droxler, A.W.**, **Bruce, C.H.**, **Sager, W.W.** and **Watkins, D.H.** (1988) Pliocene-Pleistocene variations in aragonite content and planktonic oxygen-isotope record in Bahamian periplatform ooze, Hole 633A. In: *Proc. ODP Sci. Results* (Eds Austin Jr, J.A., Schlager, W. et al.), **101**, 221–224.

**Drzewiecki, P.A.** and **Simo, J.A.** (2000) Tectonic, eustatic and environmental controls on mid-Cretaceous carbonate platform deposition, south-central Pyrenees, Spain. *Sedimentology*, **47**, 471–495.

**Eberli, G.P.**, **Bernoulli, D.**, **Sanders, D.** and **Vecsei, A.** (1993) From aggradation to progradation: The Maiella Platform, Abruzzi, Italy: Chapter 18. In: *Cretaceous Carbonate Platforms* (Eds Simo, T., Scott, R.W. and Masse, J.P.), *AAPG Mem.*, **56**, 213–232.

**Eberli, G.P.** and **Ginsburg, R.N.** (1987) Segmentation and coalescence of Cenozoic carbonate platforms, northwestern Great Bahama Bank. *Geology*, **15**, 75–79.

**Everts, A.J.W.**, **Schlager, W.** and **Reijmer, J.J.G.** (1999) Carbonate platform-to-basin correlation by means of grain-composition logs: an example from the Vercors (Cretaceous, SE France). *Sedimentology*, **46**, 261–278.

**Enos, P.** (1974) *Surface Sediment Facies of the Florida-Bahamas Plateau Map Series MC-5 no.*, 4th edn. Geological Society of America, Boulder, Colorado.

**Ericson, D.B.** and **Wollin, G.** (1968) Pleistocene climates and chronology in deep-sea sediments. *Science*, **162**, 1227.

**Ericson, D.B.**, **Ewing, M.** and **Wollin, G.** (1964) The Pleistocene Epoch in deep-sea sediments. *Science*, **146**, 723–732.

**ESRI** (2020) *ArcGIS Desktop: Release 10*. Environmental Systems Research Institute, Redlands, California.

**Fabregas, N.**, **Mulder, T.**, **Gillet, H.**, **Recouvreur, A.**, **Busson, J.**, **Hanquiez, V.** and **Borgomano, J.** (2018) Glissements sous-marins sur la pente d'Exuma Sound (Bahamas). *Réunion des Sciences de la Terre*, Earth Science Meeting (Lille).

**Fairbanks, R.G.** and **Matthews, R.K.** (1978) The marine oxygen isotope record in Pleistocene coral, Barbados, West Indies. *Quatern. Res.*, **10**, 181–196.

**Fallgatter, C.**, **Kneller, B.**, **Paim, P.S.G.** and **Milana, J.P.** (2017) Transformation, partitioning and flow–deposit interactions during the run-out of megaflows. *Sedimentology*, **64**, 359–387.

**Fauquembergue, K.**, **Ducassou, E.**, **Mulder, T.**, **Hanquiez, V.**, **Perello, M.-C.**, **Poli, E.** and **Borgomano, J.** (2018) Genesis and growth of a carbonate Holocene wedge on the northern Little Bahama Bank. *Mar. Petrol. Geol.*, **96**, 602–614.

**Ferguson, R.I.** and **Church, M.** (2004) A simple universal equation for grain settling velocity. *J. Sed. Res.*, **74**, 933–937.

**Fichtel, L.** and **Moll, J.P.C.** (1798) *Testacea microscopic alique minuta ex Generibus Argonauta et Nautilus*. Anton Pichler, Wien.

**Fildani, A.**, **Hubbard, S.M.**, **Covault, J.A.**, **Maier, K.L.**, **Romans, B.W.**, **Traer, M.** and **Rowland, J.C.** (2013) Erosion at inception of deep-sea channels. *Mar. Petrol. Geol.*, **41**, 48–61.

**Floquet, M.** and **Hennuy, J.** (2003) Evolutionary gravity flow in the middle Turonian – early Coniacian Southern Provence Basin (Se France): origins and depositional processes. In: *Submarine Mass Movements and Their Consequences. Advances in Natural and Technological Hazards Research* (Eds Locat, J., Mienert, J. and Boisvert, L.), **19**. Springer, Dordrecht, the Netherlands. https://doi.org/10.1007/978-94-010-0093-2_46

**Fouke, B.W.**, **Everts, A.-J.-W.**, **Zwart, E.W.**, **Schlager, W.**, **Smalley, P.C.** and **Weissert, H.** (1996) Subaerial exposure unconformities on the Vercors carbonate platform (SE France) and their sequence stratigraphic significance. In: *High Resolution Sequence Stratigraphy: Innovations and Applications* (Eds Howell, J.A. and Aitken, J.F.), *Geol. Soc. London Spec. Publ.*, **104**, 295–319.

**Garcia, M.** and **Parker, G.** (1989) Experiments on hydraulic jumps in turbidity currents near a canyon-fan transition. *Science*, **245**, 393.

**Guiastrennec-Faugas, L.**, **Gillet, H.**, **Silva Jacinto, R.**, **Dennielou, B.**, **Hanquiez, V.**, **Schmidt, S.**, **Simplet, L.** and **Rousset, A.** (2020) Upstream migrating knickpoints and related sedimentary processes in a submarine canyon from a rare 20-year morphobathymetric time-lapse (Capbreton submarine canyon, Bay of Biscay, France). *Mar. Geol.*, **423**, 106143.

**Grammer, G.M.** and **Ginsburg, R.N.** (1992) Highstand versus lowstand deposition on carbonate platform margins: insight from Quaternary foreslopes in the Bahamas. *Mar. Geol.*, **103**, 125–136.

**Gray, T.E.**, **Alexander, J.** and **Leeder, M.R.** (2005) Quantifying velocity and turbulence structure in depositing sustained turbidity currents across breaks in slope. *Sedimentology*, **52**, 467–488.

**Grosheny, D.**, **Ferry, S.** and **Courjault, T.** (2015) Progradational patterns at the head of single units of base-of-slope, submarine granular flow deposits ("Conglomérats des Gâs", Coniacian, SE France). *Sed. Geol.*, **317**, 102–115.

**Haak, A.B.** and **Schlager, W.** (1989) Compositional variations in calciturbidites due to sea-level fluctuations, late Quaternary, Bahamas. *Geol. Rundsch.*, **78**, 477–486.

**Hairabian, A.**, **Borgomano, J.**, **Masse, J.-P.** and **Nardon, S.** (2015) 3-D stratigraphic architecture, sedimentary processes and controlling factors of Cretaceous deep-water resedimented carbonates (Gargano Peninsula, SE Italy). *Sed. Geol.*, **317**, 116–136.

**Hampton, M.A.** (1972) The role of subaqueous debris flow in generating turbidity currents. *J. Sed. Res.*, **42**, 775–793.

**Haughton, P.**, **Davis, C.**, **McCaffrey, W.** and **Barker, S.** (2009) Hybrid sediment gravity flow deposits – classification, origin and significance. *Mar. Petrol. Geol.*, **26**, 1900–1918.

**Haughton, P.D.W.**, **Barker, S.P.** and **McCaffrey, W.D.** (2003) 'Linked' debrites in sand-rich turbidite systems – origin and significance. *Sedimentology*, **50**, 459–482.

**Heerema, C.J.**, **Talling, P.J.**, **Cartigny, M.J.**, **Paull, C.K.**, **Bailey, L.**, **Simmons, S.M.**, **Parsons, D.R.**, **Clare, M.A.**, **Gwiazda, R.**, **Lundsten, E.**, **Anderson, K.**, **Maier, K.L.**, **Xu, J.P.**, **Sumner, E.J.**, **Rosengerger, K.**, **Gales, J.**, **McGann, M.**, **Carter, L.** and **Pope, E.** (2020) What determines the downstream evolution of turbidity currents? *Earth Planet. Sci. Lett.*, **532**, 116023.

**Heezen, B.C.** and **Ewing, M.** (1952) Turbidity currents and submarine slumps, and the 1929 Grand Banks earthquake. *Am. J. Sci.*, **250**, 849–873.

**Heiniö, P.** and **Davies, R.J.** (2007) Knickpoint migration in submarine channels in response to fold growth, western Niger Delta. *Mar. Petrol. Geol.*, **24**, 434–449.

**Herbig, H.G.** and **Mamet, B.** (1994) Hydraulic sorting of microbiota in calciturbidites – a Dinantian case study from the Rheinische Schiefergebirge, Germany. *Facies*, **31**, 93–104.

**Hine, A.C.**, **Wilber, R.J.**, **Bane, J.M.**, **Neumann, A.C.** and **Lorenson, K.R.** (1981) Offbank transport of carbonate sands along open, leeward bank margins: Northern Bahamas. *Mar. Geol.*, **42**, 327–348.

**Hiscott, R.N.** (1994) Loss of capacity, not competence, as the fundamental process governing deposition from turbidity currents. *J. Sed. Res.*, **64**, 209–214.

**Hodson, J.M.** and **Alexander, J.** (2010) The effects of grain-density variations on turbidity currents and some implications for the deposition of carbonate turbidites. *J. Sed. Res.*, **80**, 515–528.

**Hofstra, M.**, **Hodgson, D.M.**, **Peakall, J.** and **Flint, S.S.** (2015) Giant scour-fills in ancient channel-lobe transition zones: Formative processes and depositional architecture. *Sed. Geol.*, **329**, 98–114.

**Hubbard, S.M.**, **Covault, J.A.**, **Fildani, A.** and **Romans, W.** (2014) Sediment transfer and deposition in slope channels: Deciphering the record of enigmatic deep-sea processes from outcrop. *Geol. Coc. Am. Bull.*, **126**, 857–871.

**Hughes Clarke, J.E.** (2016) First wide-angle view of channelized turbidity currents links migrating cyclic steps to flow characteristics. *Nat. Commun.*, **7**, 11896.

**Jo, A.**, **Eberli, G.P.** and **Grasmueck, M.** (2015) Margin collapse and slope failure along southwestern Great Bahama Bank. *Sed. Geol.*, **317**, 43–52.

**Jorry, S.J.**, **Droxler, A.W.** and **Francis, J.M.** (2010) Deepwater carbonate deposition in response to re-flooding of carbonate bank and atoll-tops at glacial terminations. *Quatern. Sci. Rev.*, **29**, 2010–2026.

**Kendall, C.G.S.C.** and **Schlager, W.** (1981) Carbonates and relative changes in sea level. *Mar. Geol.*, **44**, 181–212.

**Kier, J.S.** and **Pilkey, O.H.** (1971) The influence of sea level changes on sediment carbonate mineralogy, Tongue of the Ocean, Bahamas. *Mar. Geol.*, **11**, 189–200.

**Kleverlaan, K.** (1987) Gordo megabed: a possible seismite in a Tortonian submarine fan, Tabernas Basin, province Almeria, southeast Spain. *Sed. Geol.*, **51**, 165–180.

**Kneller, B.** and **Buckee, C.** (2000) The structure and fluid mechanics of turbidity currents: a review of some recent studies and their geological implications. *Sedimentology*, **47**, 62–94.

**Koch, R.** (1923) Die jungtertiare Foraminiferen fauna von Kabu (Res. Surbaja Java). *Eclogae Geol. Helv.*, **18**, 342–357.

**Komar, P.D.** (1971) Hydraulic jumps in turbidity currents. *Geol. Soc. Am. Bull.*, **82**, 1477–1488.

**Krause, F.F.** and **Oldershaw, A.E.** (1979) Submarine carbonate breccia beds—a oppositional model for two-layer, sediment gravity flows from the Sekwi Formation (Lower Cambrian), Mackenzie Mountains, Northwest Territories, Canada. *Can. J. Earth Sci.*, **16**, 189–199.

**Kuenen, P.H.** and **Migliorini, C.I.** (1950) Turbidity currents as a cause of graded bedding. *J. Geol.*, **58**, 91–127.

**Labaume, P.**, **Mutti, E.** and **Seguret, M.** (1987) Megaturbidites: a depositional model from the Eocene of the SW-Pyrenean Foreland basin, Spain. *Geo-Mar. Lett.*, **7**, 91–101.

**Lambeck, K.**, **Antonioli, F.**, **Anzidei, M.**, **Ferranti, L.**, **Leoni, G.**, **Scicchitano, G.** and **Silenzi, S.** (2011) Sea level change along the Italian coast during the Holocene and projections for the future. *Quatern. Int.*, **232**, 250–257.

**Laugié, M.**, **Michel, J.**, **Pohl, A.**, **Poli, E.** and **Borgomano, J.** (2019) Global distribution of modern shallow-water marine carbonate factories: a spatial model based on environmental parameters. *Sci. Rep.*, **9**, 16432.

**Le Goff, J.**, **Cerepi, A.**, **Swennen, R.**, **Loisy, C.**, **Caron, M.**, **Muska, K.** and **El Desouky, H.** (2015) Contribution to the understanding of the Ionian Basin sedimentary evolution along the eastern edge of Apulia during the Late Cretaceous in Albania. *Sed. Geol.*, **317**, 87–101.

**Le Goff, J.**, **Reijmer, J.J.G.**, **Cerepi, A.**, **Loisy, C.**, **Swennen, R.**, **Heba, G.**, **Cavailhes, T.** and **De Graaf, S.** (2019) The dismantling of the Apulian carbonate platform during the late Campanian – early Maastrichtian in Albania. *Cretaceous Res.*, **96**, 83–106.

**Liu, J.P.** and **Milliman, J.D.** (2004) Reconsidering melt-water pulses 1A and 1B: Global impacts of rapid sea-level rise. *J. Ocean Univ. China*, **3**, 183–190.

**Macdonald, H.A.**, **Wynn, R.B.**, **Huvenne, V.A.I.**, **Peakall, J.**, **Masson, D.G.**, **Weaver, P.P.E.** and **McPhail, S.D.** (2011) New insights into the morphology, fill, and remarkable longevity (>0.2 m.y.) of modern deep-water erosional scours along the northeast Atlantic margin. *Geosphere*, **7**, 845–867.

**Maiklem, W.R.** (1968) Some hydraulic properties of bioclastic carbonate grains. *Sedimentology*, **10**, 101–109.

**Mayall, M.**, **Jones, E.** and **Casey, M.** (2006) Turbidite channel reservoirs—key elements in facies prediction and effective development. *Mar. Petrol. Geol.*, **23**, 821–841.

**McCave, I.N.** (1972) Transport and escape of fine-grained sediment from shelf areas. In: *Shelf Sediment Transport* (Eds Swift, D.J.P., Duane, D. and Pilkey, O.H.), pp. 225–248. Dowden Hutchinson and Ross, Stroudsburg, PA.

**McIlreath, L.A.** and **James, N.P.** (1978) Carbonate slopes. In: *Facies Models. Geoscience Canada*, **5**, 189–199.

**Michel, J.**, **Borgomano, J.** and **Reijmer, J.J.G.** (2018) Heterozoan carbonates: When, where and why? A synthesis on parameters controlling carbonate production and occurrences. *Earth-Sci. Rev.*, **182**, 50–67.

**Migeon, S.**, **Weber, O.**, **Faugeres, J.-C.** and **Saint-Paul, J.** (1998) SCOPIX: a new X-ray imaging system for core analysis. *Geo-Mar. Lett.*, **18**, 251–255.

**Mindszenty, A.**, **D'Argenio, B.** and **Aiello, G.** (1995) Lithospheric bulge-related uplift as recorded by regional uncomformities-the case of Apulia. *Tectonophysics*, **252**, 137–161.

**Mitchell, N.C.** (2004) Form of submarine erosion from confluences in Atlantic USA continental slope Canyons. *Am. J. Sci.*, **304**, 590–611.

**Mitchell, N.C.** (2006) Morphologies of knickpoints in submarine canyons. *Geol. Soc. Am. Bull.*, **118**, 589–605.

**Mulder, T.** and **Alexander, J.** (2001a) Abrupt change in slope causes variation in the deposit thickness of concentrated particle-driven density-currents. *Mar. Geol.*, **175**, 221–235.

**Mulder, T.** and **Alexander, J.** (2001b) The physical character of subaqueous sedimentary density flows and their deposits. *Sedimentology*, **48**, 269–299.

**Mulder, T.**, **Ducassou, E.**, **Eberli, G.P.**, **Hanquiez, V.**, **Gonthier, E.**, **Kindler, P.**, **Principaud, M.**, **Fournier, F.**, **Léonide, P.**, **Billeaud, I.**, **Marsset, B.**, **Reijmer, J.J.G.**, **Bondu, C.**, **Joussiaume, R.** and **Pakiades, M.** (2012) New insights into the morphology and sedimentary processes along the western slope of Great Bahama Bank. *Geology*, **40**, 603–606.

**Mulder, T.**, **Ducassou, E.**, **Gillet, H.**, **Hanquiez, V.**, **Principaud, M.**, **Chabaud, L.**, **Eberli, G.P.**, **Kindler, P.**, **Billeaud, I.**, **Gonthier, E.**, **Fournier, F.**, **Léonide, P.** and **Borgomano, J.** (2014) First discovery of channel-levee complexes in a modern deep-water carbonate slope environment. *J. Sed. Res.*, **84**, 1139–1146.

**Mulder, T.**, **Joumes, M.**, **Hanquiez, V.**, **Gillet, H.**, **Reijmer, J.J.G.**, **Tournadour, E.**, **Chabaud, L.**, **Principaud, M.**, **Schnyder, J.S.D.**, **Borgomano, J.**, **Fauquembergue, K.**, **Ducassou, E.** and **Busson, J.** (2017) Carbonate slope morphology revealing sediment transfer from bank-to-slope (Little Bahama Bank, Bahamas). *Mar. Petrol. Geol.*, **83**, 26–34.

**Mulder, T.**, **Gillet, H.**, **Hanquiez, V.**, **Ducassou, E.**, **Fauquembergue, K.**, **Principaud, M.**, **Conesa, G.**, **Le Goff, J.**, **Ragusa, J.**, **Bashah, S.**, **Bujan, S.**, **Reijmer, J.J.G.**, **Cavailhes, T.**, **Droxler, A.W.**, **Blank, D.G.**, **Guiastrennec, L.**, **Fabregas, N.**, **Recouvreur, A.** and **Seibert, C.** (2018) Carbonate slope morphology revealing a giant submarine canyon (Little Bahama Bank, Bahamas). *Geology*, **46**, 31–34.

**Mulder, T.**, **Gillet, H.**, **Hanquiez, V.**, **Reijmer, J.J.G.**, **Droxler, A.W.**, **Recouvreur, A.**, **Fabregas, N.**, **Cavailhes, T.**, **Fauquembergue, K.**, **Blank, D.G.**, **Guiastrennec, L.**, **Seibert, C.**, **Bashah, S.**, **Bujan, S.**, **Ducassou, E.**, **Principaud, M.**, **Conesa, G.**, **Le Goff, J.**, **Ragusa, J.**, **Busson, J.** and **Borgomano, J.** (2019) Into the deep: a coarse-grained carbonate turbidite valley and canyon in ultra-deep carbonate setting. *Mar. Geol.*, **407**, 316–333.

**Mullins, H.T.** and **Cook, H.E.** (1986) Carbonate apron models: alternatives to the submarine fan model for paleoenvironmental analysis and hydrocarbon exploration. *Sed. Geol.*, **48**, 37–79.

**Mullins, H.T.**, **Heath, K.C.**, **Van Buren, H.M.** and **Newton, C.R.** (1984) Anatomy of a modern open-ocean carbonate slope: northern Little Bahama Bank. *Sedimentology*, **31**, 141–168.

**Mylroie, J.E.** and **Carew, J.L.** (1995) Geology and karst geomorphology of the San Salvador Island, Bahamas. *Carbonates Evaporites*, **10**, 193–206.

**d'Orbigny, A.** (1839) Foraminifères des Iles Canaries. In: *Histoire Naturelle Des Iles Canaries* (Eds Barker-Webb, P. and Berthelot, S.), **2**, 120–146.

**Parker, G.** and **Izumi, N.** (2000) Purely erosional cyclic and solitary steps created by flow over a cohesive bed. *J. Fluid Mech.*, **419**, 203–238.

**Parker, W.K.** and **Jones, T.R.** (1865) On some foraminifera from the North Atlantic and Artic Oceans, including Davis Straits and Baffin's Bay. *Phil. Trans. Roy. Soc. London*, **155**, 325–441.

**Paul, A.**, **Reijmer, J.J.G.**, **Fürstenau, J.**, **Kinkel, H.** and **Betzler, C.** (2012) Relationship between Late Pleistocene sea-level variations, carbonate platform morphology and aragonite production (Maldives, Indian Ocean). *Sedimentology*, **59**, 1640–1658.

**Payros, A.** and **Pujalte, V.** (2008) Calciclastic submarine fans: an integrated overview. *Earth-Sci. Rev.*, **86**, 203–246.

**Payros, A.**, **Pujalte, V.** and **Orue-Etxebarria, X.** (1999) The South Pyrenean Eocene carbonate megabreccias revisited: new interpretation based on evidence from the Pamplona Basin. *Sed. Geol.*, **125**, 165–194.

**Pilskaln, C.H.**, **Neumann, A.C.** and **Bane, J.M.** (1989) Periplatform carbonate flux in the northern Bahamas. *Deep Sea Res. A. Oceanogr. Res. Pap.*, **36**, 1391–1406.

**Pohl, F.** (2019) Turbidity currents and their deposits in abrupt morphological transition zones. PhD Thesis, University of Utrecht, 205 pp.

**Pohl, F.**, **Eggenhuisen, J.T.**, **Tilston, M.** and **Cartigny, M.J.B.** (2019) New flow relaxation mechanism explains scour fields at the end of submarine channels. *Nat. Commun.*, **10**, 4425.

**Posamentier, H.W.** and **Kolla, V.** (2003) Seismic geomorphology and stratigraphy of depositional elements in deep-water settings. *J. Sed. Res.*, **73**, 367–388.

**Postma, G.** and **Cartigny, M.J.B.** (2014) Supercritical and subcritical turbidity currents and their deposits—a synthesis. *Geology*, **42**, 987–990.

**Principaud, M.**, **Mulder, T.**, **Gillet, H.** and **Borgomano, J.** (2015) Large-scale carbonate submarine mass-wasting along the northwestern slope of the Great Bahama Bank (Bahamas); morphology, architecture, and mechanisms. *Sed. Geol.*, **317**, 27–42.

**Principaud, M.**, **Ponte, J.-P.**, **Mulder, T.**, **Gillet, H.**, **Robin, C.** and **Borgomano, J.** (2016) Slope-to-basin stratigraphic evolution of the northwestern Great Bahama Bank (Bahamas) during the Neogene to Quaternary: interactions between downslope and bottom currents deposits. *Basin Res.*, **29**, 699–724.

**Puga-Bernabéu, Á.**, **Webster, J.M.**, **Beaman, R.J.** and **Guilbaud, V.** (2011) Morphology and controls on the evolution of a mixed carbonate–siliciclastic submarine canyon system, Great Barrier Reef margin, north-eastern Australia. *Mar. Geol.*, **289**, 100–116.

**Puga-Bernabéu, Á.**, **Webster, J.M.**, **Beaman, R.J.** and **Guilbaud, V.** (2013) Variation in canyon morphology on the Great Barrier Reef margin, north-eastern Australia: the influence of slope and barrier reefs. *Geomorphology*, **191**, 35–50.

**Purdy, E.G.** (1963) Recent calcium carbonate facies of the Great Bahama Bank. 1. Petrography and reaction groups. *J. Geol.*, **71**, 334–355.

**Rama-Corredor, O.**, **Martrat, B.**, **Grimalt, J.O.**, **Lopez-Otalvaro, G.E.**, **Flores, J.A.** and **Sierro, F.** (2015) Parallelisms between sea surface temperature changes in the western tropical Atlantic (Guiana Basin) and high latitude climate signals over the last 140 000 years. *Clim. Past*, **11**, 1297–1311.

**Rankey, E.C.** and **Doolittle, D.F.** (2012) Geomorphology of carbonate platform-marginal uppermost slopes: insights from a Holocene analogue, Little Bahama Bank, Bahamas. *Sedimentology*, **59**, 2146–2171.

**Rankey, E.C.**, **Enos, P.**, **Steffen, K.** and **Druke, D.** (2004) Lack of impact of hurricane Michelle on tidal flats, Andros Island, Bahamas: integrated remote sensing and field observations. *J. Sed. Res.*, **74**, 654–661.

**Rankey, E.C.** and **Reeder, S.L.** (2011) Holocene oolitic marine sand complexes of the Bahamas. *J. Sed. Res.*, **81**, 97–117.

**Rebotim, A.**, **Voelker, A.H.L.**, **Jonkers, L.**, **Waniek, J.J.**, **Meggers, H.**, **Schiebel, R.**, **Fraile, I.**, **Schulz, M.** and **Kucera, M.** (2017) Factors controlling the depth habitat of planktonic foraminifera in the subtropical eastern North Atlantic. *Biogeosciences*, **14**, 827–859.

**Recouvreur, A.** (2017) Analyse de la morphobathymétrie, des données acoustiques et de la sismique Très Haute Résolution du canyon d'Exuma (Bahamas). MSc Thesis, University of Bordeaux, 43 pp.

**Reeder, S.L.** and **Rankey, E.C.** (2009) A tale of two storms: an integrated field, remote sensing and modelling study examining the impact of hurricanes frances and jeanne on carbonate systems, Bahamas. In: *Perspectives in Carbonate Geology* (Eds Swart, P.K., Eberli, G.P. and McKenzie, J.A.), *IAS Special Publication*, **41**, 75–90. International Association of Sedimentologists – Blackwell Publishing Ltd., Chichester, UK.

**Reijmer, J.J.G.**, **Palmieri, P.** and **Groen, R.** (2012) Compositional variations in calciturbidites and calcidebrites in response to sea-level fluctuations (Exuma Sound, Bahamas). *Facies*, **58**, 493–507.

**Reijmer, J.J.G.**, **Palmieri, P.**, **Groen, R.** and **Floquet, M.** (2015) Calciturbidites and calcidebrites: sea-level variations or tectonic processes? *Sed. Geol.*, **317**, 53–70.

**Reijmer, J.J.G.**, **Schlager, W.**, **Bosscher, H.**, **Beets, C.J.** and **McNeill, D.F.** (1992) Pliocene/Pleistocene platform facies transition recorded in calciturbidites (Exuma Sound, Bahamas). *Sed. Geol.*, **78**, 171–179.

**Reijmer, J.J.G.**, **Slootman, A.**, **de Kruijf, M.**, **de Boer, R.A.** and **Kranenburg, J.** (2019) From grain to flume tank: analyzing the hydrodynamic behaviour of carbonate sediments. AAPG ACE-2019, San Antonio, USA.

**Reijmer, J.J.G.**, **Swart, P.K.**, **Bauch, T.**, **Otto, R.**, **Reuning, L.**, **Roth, S.** and **Zechel, S.** (2009) A re-evaluation of facies on Great Bahama Bank I: new facies maps of western Great Bahama Bank. In: *Perspectives in Carbonate Geology: A Tribute to the Career of Robert Nathan Ginsburg* (Eds Swart, P.K., Eberli, G.P. and McKenzie, J.A.), *Special Publication Int. Assoc. Sedimentol.*, 41, 29–46. Wiley-Blackwell-IAS, Oxford.

**Reimer, P.J.**, **Bard, E.**, **Bayliss, A.**, **Beck, J.W.**, **Blackwell, P.G.**, **Ramsey, C.B.**, **Buck, C.E.**, **Cheng, H.**, **Edwards, R.L.**, **Friedrich, M.**, **Grootes, P.M.**, **Guilderson, T.P.**, **Haflidason, H.**, **Hajdas, I.**, **Hatté, C.**, **Heaton, T.J.**, **Hoffmann, D.L.**, **Hogg, A.G.**, **Hughen, K.A.**, **Kaiser, K.F.**, **Kromer, B.**, **Manning, S.W.**, **Niu, M.**, **Reimer, R.W.**, **Richards, D.A.**, **Scott, E.M.**, **Southon, J.R.**, **Staff, R.A.**, **Turney, C.S.M.** and **Plicht, J.v.d.**, (2013) IntCal13 and Marine13 radiocarbon age calibration curves 0–50,000 years cal BP. *Radiocarbon*, **55**, 1869–1887.

**Rendle, R.H.** and **Reijmer, J.J.G.** (2002) Quaternary slope development of the western, leeward margin of the Great Bahama Bank. *Mar. Geol.*, **185**, 143–164.

**Rendle-Bühring, R.H.** and **Reijmer, J.J.G.** (2005) Controls on grain-size patterns in periplatform carbonates: Marginal setting versus glacio-eustacy. *Sed. Geol.*, **175**, 99–113.

**Reymer, J.J.G.**, **Schlager, W.** and **Droxler, A.W.** (1988) Site 632: Pliocene-Pleistocene sedimentation cycles in a Bahamian basin. In: *Proceedings of the Ocean Drilling Program*, Scientific Results Leg 101, Volume 101 (Eds Austin Jr, J.A. and Schlager, W., et al.), Ocean Drilling Program, College Station, TX, 213–220.

**Roth, S.** and **Reijmer, J.J.G.** (2004) Holocene Atlantic climate variations deduced from carbonate periplatform sediments (leeward margin, Great Bahama Bank). *Paleoceanography*, **19**, 1–14.

**Roth, S.** and **Reijmer, J.J.G.** (2005) Holocene millennial to centennial carbonate cyclicity recorded in slope sediments of the Great Bahama Bank and its climatic implications. *Sedimentology*, **52**, 161–181.

**Ruiz-Ortiz, P.A.**, **Bosence, D.W.J.**, **Rey, J.**, **Nieto, L.M.**, **Castro, J.M.** and **Molina, J.M.** (2004) Tectonic control of facies architecture, sequence stratigraphy and drowning of a Liassic carbonate platform (Betic Cordillera, Southern Spain). *Basin Res.*, **16**, 235–257.

**Rusnak, G.A.** and **Nesteroff, W.D.** (1964) Modern turbidites: Terrigenous abyssal plain versus bioclastic basin. In: *Papers in Marine Geology, Shepard Commemorative Volume* (Ed. Miller, L.R.), pp. 488–503. Macmillan, New York.

**Savary, B.** and **Ferry, S.** (2004) Geometry and petrophysical parameters of a calcarenitic turbidite lobe (Barremian-Aptian, Pas-de-la-Cluse, France). *Sed. Geol.*, **168**, 281–304.

**Schlager, W.** (2005) *Carbonate Sedimentology and Sequence Stratigraphy*. SEPM. Concepts in Sedimentology and Paleontology. SEPM (Society for Sedimentary Geology), Tulsa, Oklahoma, **8**, 200 pp.

**Schlager, W.** (1981) The paradox of drowned reefs and carbonate platforms. *Geol. Soc. Am. Bull.*, **92**, 197–211.

**Schlager, W.** and **Ginsburg, R.N.** (1981) Bahama carbonate platforms — The deep and the past. *Mar. Geol.*, **44**, 1–24.

**Schlager, W.**, **Reijmer, J.J.G.** and **Droxler, A.** (1994) Highstand shedding of carbonate platforms. *J. Sed. Res.*, **64**, 270–281.

**Simpson, J.E.** (1969) A comparison between laboratory and atmospheric density currents. *Q. J. Roy. Meteorol. Soc.*, **95**, 758–765.

**Slootman, A.** and **Cartigny, M.J.B.** (2020) Cyclic steps: Review and aggradation-based classification. *Earth-Sci. Rev.*, **201**, 102949.

**Slootman, A.**, **De Kruijf, M.**, **Yong, G.**, **Eggenhuisen, J.** and **Reijmer, J.J.G.** (2019) Hydraulics of carbonate grains: Insights from settling tube and flume experiments. *Bathurst Meeting of Carbonate Sedimentologists 2019*, Palma de Mallorca, Spain.

**Spence, G.H.** and **Tucker, M.E.** (1997) Genesis of limestone megabreccias and their significance in carbonate sequence stratigraphic models: a review. *Sed. Geol.*, **112**, 163–193.

**Stuiver, M.**, **Reimer, P.J.** and **Reimer, R.W.** (2013) CALIB 7.0.4 [WWW program]. Available at: http://calib.org

**Szulczewski, M.**, **Belka, Z.** and **Skompski, S.** (1996) The drowning of a carbonate platform: an example from the Devonian-Carboniferous of the southwestern Holy Cross Mountains, Poland. *Sed. Geol.*, **106**, 21–49.

**Talling, P.J.**, **Amy, L.A.**, **Wynn, R.B.**, **Peakall, J.** and **Robinson, M.** (2004) Beds comprising debrite sandwiched within co-genetic turbidite: origin and widespread occurrence in distal depositional environments. *Sedimentology*, **51**, 163–194.

**Talling, P.J.**, **Masson, D.G.**, **Sumner, E.J.** and **Malgesini, G.** (2012) Subaqueous sediment density flows: depositional processes and deposit types. *Sedimentology*, **59**, 1937–2003.

**Toniolo, H.** and **Cantelli, A.** (2007) Experiments on upstream-migrating submarine knickpoints. *J. Sed. Res.*, **77**, 772–783.

**Toomey, M.R.**, **Curry, W.B.**, **Donnelly, J.P.** and **van Hengstum, P.J.** (2013) Reconstructing 7000 years of North Atlantic hurricane variability using deep-sea sediment cores from the western Great Bahama Bank. *Paleoceanography*, **28**, 31–41.

**Tournadour, E.**, **Mulder, T.**, **Borgomano, J.**, **Gillet, H.**, **Chabaud, L.**, **Ducassou, E.**, **Hanquiez, V.** and **Etienne, S.** (2017) Submarine canyon morphologies and evolution in modern carbonate settings: The northern slope of Little Bahama Bank, Bahamas. *Mar. Geol.*, **391**, 76–97.

**Vigorito, M.**, **Murru, M.** and **Simone, L.** (2005) Anatomy of a submarine channel system and related fan in a foramol/rhodalgal carbonate sedimentary setting: a case history from the Miocene syn-rift Sardinia Basin, Italy. *Sed. Geol.*, **174**, 1–30.

**Webster, J.M.**, **Braga, J.C.**, **Humblet, M.**, **Potts, D.C.**, **Iryu, Y.**, **Yokoyama, Y.**, **Fujita, K.**, **Bourillot, R.**, **Esat, T.M.**, **Fallon, S.**, **Thompson, W.G.**, **Thomas, A.L.**, **Kan, H.**, **McGregor, H.V.**, **Hinestrosa, G.**, **Obrochta, S.P.** and **Lougheed, B.C.** (2018) Response of the Great Barrier Reef to sea-level and environmental changes over the past 30,000 years. *Nat. Geosci.*, **11**, 426–432.

**Wilber, R.J.**, **Milliman, J.D.** and **Halley, R.B.** (1990) Accumulation of bank-top sediment on the western slope of Great Bahama Bank: rapid progradation of a carbonate megabank. *Geology*, **18**, 970–974.

**Wilson, P.A.** and **Roberts, H.H.** (1992) Carbonate-periplatform sedimentation by density flows: a mechanism for rapid off-bank and vertical transport of shallow-water fines. *Geology*, **20**, 713–716.

**Wilson, P.A.** and **Roberts, H.H.** (1995) Density cascading; off-shelf sediment transport, evidence and implications, Bahama Banks. *J. Sed. Res.*, **A65**, 45–56.

**Wunsch, M.**, **Betzler, C.**, **Eberli, G.P.**, **Lindhorst, S.**, **Lüdmann, T.** and **Reijmer, J.J.G.** (2018) Sedimentary dynamics and high-frequency sequence stratigraphy of the southwestern slope of Great Bahama Bank. *Sed. Geol.*, **363**, 96–117.

**Wynn, R.B.**, **Kenyon, N.H.**, **Masson, D.G.**, **Stow, D.A.V.** and **Weaver, P.P.E.** (2002) Characterization and recognition of deep-water channel-lobe transition zones. *AAPG Bull.*, **86**, 1441–1462.

**Zhang, L.**, **Iwasaki, T.**, **Li, T.**, **Fu, X.**, **Wang, G.** and **Parker, G.** (2019) Bedrock-alluvial streams with knickpoint and plunge pool that migrate upstream with permanent form. *Sci. Rep.*, **9**, 6176.

*Manuscript received 3 April 2020; revision accepted 31 July 2020*